Submitted to Acta Metallurgica

UCRL-18840
Preprint

cy. 2

STRUCTURE AND PROPERTIES OF SPINODALLY DECOMPOSED Cu-Ni-Fe ALLOYS

Ernest Paul Butler

June 1969

AEC Contract No. W-7405-eng-48

TWO-WEEK LOAN COPY

This is a Library Circulating Copy
which may be borrowed for two weeks.
For a personal retention copy, call
Tech. Info. Division, Ext. 5545

LAWRENCE RADIATION LABORATORY
UNIVERSITY of CALIFORNIA BERKELEY

UCRL-18840
cy. 2

DISCLAIMER

This document was prepared as an account of work sponsored by the United States Government. While this document is believed to contain correct information, neither the United States Government nor any agency thereof, nor the Regents of the University of California, nor any of their employees, makes any warranty, express or implied, or assumes any legal responsibility for the accuracy, completeness, or usefulness of any information, apparatus, product, or process disclosed, or represents that its use would not infringe privately owned rights. Reference herein to any specific commercial product, process, or service by its trade name, trademark, manufacturer, or otherwise, does not necessarily constitute or imply its endorsement, recommendation, or favoring by the United States Government or any agency thereof, or the Regents of the University of California. The views and opinions of authors expressed herein do not necessarily state or reflect those of the United States Government or any agency thereof or the Regents of the University of California.

UNIVERSITY OF CALIFORNIA

Lawrence Radiation Laboratory
Berkeley, California

June 5, 1970

ERRATA

TO: All recipients of UCRL-18840

FROM: Technical Information Division

SUBJECT: UCRL-18840: Structure and Properties of Spinodally Decomposed Cu-Ni-Fe Alloys, Ernest Paul Butler and Gareth Thomas, June 1969

Please make the following corrections on subject report:

Page 8, line 16: recipitation should read precipitation

Page 14, line 6 from bottom of page: Alignments should read Alignment

Page 15, line 17, 18, 20, 22, 23: σ should read δ

Page 17, $[\gamma_1 + \gamma_2]' \rightarrow [\gamma_1 + \gamma_2]'' \rightarrow [\gamma_1 + \gamma_2]$

Page 18, line 6: Thus the mechanism should read Thus if the mechanism...

line 8: (from bottom) add 'a' to read a consequence...

Page 20, line 5: (from bottom) along should read alone...

Page 27, line 7: should read or not of...

line 7: omit 'by' at end of line

Page 33: second formula - add brackets to formula.

Please insert attached Abstract to your copy of subject report.

STRUCTURE AND PROPERTIES OF SPINODALLY DECOMPOSED Cu-Ni-Fe ALLOYS

Ernest Paul Butler* and Gareth Thomas

Inorganic Materials Research Division, Lawrence Radiation Laboratory
Department of Materials Science and Engineering, College of Engineering,
University of California, Berkeley, California

ABSTRACT

This investigation is concerned with the structural spinodal decomposition and accompanying changes in properties of a 51.5 Cu-33.5 Ni-15.0 Fe alloy after solution treatment and fast quenching. Transmission electron microscopy and diffraction, and magnetic analysis were the principal techniques employed. During aging the two-phase microstructure coarsens such that the mean wavelength is determined by a $(\text{time})^{1/3}$ law. Eventually, coherency is lost when $\lambda \sim 1000\text{Å}$, interfacial dislocations with $\bar{b} = a/2 \langle 110 \rangle$ are created and the coarsening rate is accelerated. During loss of coherency there is a change to tetragonal symmetry and then cubic again once the interface consists of a complete network of dislocations. Magnetic measurements show that the changes in composition during the spinodal transformation occur very rapidly and are best described by square wave fluctuations along $\langle 100 \rangle$. Results of mechanical testing, Curie temperature and wavelength measurements indicate the age hardening response is controlled principally by the difference in lattice parameter of the two phases, in agreement with the internal stress theory of Mott and Nabarro. A discussion of other theories of hardening in spinodals show that they are unable to explain the measured yield stress or its variation with aging.

---

* Now at the Department of Metallurgy, The University of Connecticut, Storrs, Connecticut, 06268.

TABLE OF CONTENTS

ABSTRACT

1. Introduction 1
2. Experimental Procedure 4
   2.1 Materials and Heat Treatment 4
   2.2 Electron Microscopy 4
   2.3 Magnetic Measurements 5
   2.4 Tensile Testing 6
3. Results 7
   3.1 Microstructure 7
      3.1.1 General Features 7
      3.1.2 Loss of Coherency 9
      3.1.3 Effect of Deformation 10
   3.2 Measurement of Wavelength 10
   3.3 Measurement of Curie Temperature and Mechanical Properties 12
4. Discussion 14
   4.1 Partial Coherency 14
   4.2 Mode and Kinetics of Decomposition 19
   4.3 Age Hardening 23
5. Summary and Conclusions 26

Acknowledgements 28
Appendix - Tests of Spinodal Hardening Theories 30
References 36
Figure Captions 38
Figures 42

STRUCTURE AND PROPERTIES OF SPINODALLY DECOMPOSED Cu-Ni-Fe ALLOYS

Ernest Paul Butler *

Inorganic Materials Research Division, Lawrence Radiation Laboratory
Department of Materials Science and Engineering, College of Engineering,
University of California, Berkeley, California

ABSTRACT

This investigation is concerned with the structural spinodal decomposition and accompanying changes in properties of a 51.5 Cu-33.5 Ni-15.0 Fe alloy after solution treatment and fast quenching. Transmission electron microscopy and diffraction, and magnetic analysis were the principal techniques employed. During aging the two-phase microstructure coarsens such that the mean wavelength is determined by a $(\text{time})^{1/3}$ law. Eventually, coherency is lost when $\lambda \sim 1000\text{Å}$, interfacial dislocations with $\bar{b} = a/2 \langle 110 \rangle$ are created and the coarsening rate is accelerated. During loss of coherency there is a change to tetragonal symmetry and then cubic again once the interface consists of a complete network of dislocations. Magnetic measurements show that the changes in composition during the spinodal transformation occur very rapidly and are best described by square wave fluctuations along $\langle 100 \rangle$. Results of mechanical testing, Curie temperature and wavelength measurements indicate the age hardening response is controlled principally by the difference in lattice parameter of the two phases, in agreement with the internal stress theory of Mott and Nabarro. A discussion of other theories of hardening in spinodals show that they are unable to explain the measured yield stress or its variation with aging.

* Now at the Department of Metallurgy, The University of Connecticut, Storrs, Connecticut, 06268.

1. INTRODUCTION

Most of the advances in our understanding of spinodal decomposition have come through the theoretical work of Hillert, Hilliard, and Cahn, and the important features of the transformation are reviewed in a recent paper by Cahn.[1]

In cubic crystals spinodal decomposition occurs along each of the three elastically "soft" cube directions, whereas in tetragonal systems such as TiO_2-SnO_2[2] only unidimensional composition fluctuations along [001] are involved. As a consequence of the elastic anisotropy, periodic structures are formed in spinodals which produce side bands in diffraction patterns and these have been widely studied by X-ray investigators. However, side bands can also be produced in alloys whose composition is not inside the spinodal curve if periodic structures develop by selective growth, e.g., Ni-Al[3] or in other cases of periodic arrangements such as occur in certain ordering systems. Spinodal decomposition also occurs in elastically isotropic systems such as Al-Zn[4] and Na_2O-SiO_2[5].

The side band phenomenon in Cu-Ni-Fe alloys was discovered by Daniel and Lipson[6] and was the subject of later X-ray investigations by Hargreaves,[7] Biedermann and Kneller[8] and Hillert et al.[9] Some electron microscopy work on Cu-Ni-Fe has been published by Nicholson and Tufton[10] and some observations related to fatigue have been reported by Ham et al.[11] Villagrana[12] utilized Lorentz electron microscopy in a study of this system. However, a detailed metallographic investigation has not yet been reported.

The microstructure of the alloy at any stage of its decomposition can be defined by three main parameters:

(1) Volume fraction of the two phases.

(2) Wavelength, λ

(3) Amplitude of the composition fluctuations, A.

The purpose of this investigation was to follow in detail the changes in these parameters during decomposition of a Cu-Ni-Fe alloy whose composition was close to that corresponding to the center of the miscibility gap. The changes in microstructure, volume fraction of phases and wavelength were followed by electron microscopy and diffraction. The composition fluctuations were deduced by measuring the Curie temperature, θ_c which could then be directly related to the changes in composition. Finally, the relationship between the above parameters and the age-hardening behavior of the alloy was investigated.

Figure 1 shows the ternary Cu-Ni-Fe equilibrium diagram. The 625°C and 775°C solubility limits and the tie-lines are taken from the work of Köster and Dannöhl[13]. Decomposition of the high temperature fcc γ phase gives a paramagnetic Cu-rich phase and a ferromagnetic Ni/Fe-rich phase both having fcc structures. The dotted tie-line which passes through alloys 1 and 2 was used by Hillert et al[9] and joins the copper corner of the diagram to the composition $Ni_{0.7}Fe_{0.3}$. The tie line X-Y used in this investigation joins alloys which have the same Curie temperature (530°C)[13] after equilibrium slow cooling.

Figure 2 is the pseudo-binary section along X-Y. The solvus curve and variation of Curie temperature with composition for quenched alloys are again taken from Köster and Dannöhls work. The position of the chemical spinodal curve was calculated from the formula derived by Cook and Hilliard[14]. This curve is the locus of points where $\delta^2F/\delta c^2 = 0$ and does not include the effect of coherency strains. However these are expected to be small in Cu-Ni-Fe (as was subsequently confirmed by

electron microscopy), probably less than the uncertainty in the position of the phase boundary.

2. EXPERIMENTAL PROCEDURE

2.1 Materials and Heat Treatment

The alloys were prepared by vacuum melting 99.999% purity Cu, 99.85% purity Ni, and 99.6% purity Fe, followed by chill casting into copper molds to minimize segregation. The compositions in at.% found by chemical analysis were: alloy 1, 51.5 Cu-33.5 Ni-15.0 Fe; alloy 2, 70 Cu-21Ni-9Fe. After homogenization, slices were cut from the ingot and cold-rolled with intermediate annealing until a final thickness of 300μ was reached. Strip material for electron microscopy was further reduced to 200μ thickness.

The specimens were solution-treated at 1050°C for two hours in evacuated quartz tubes and then quenched by breaking the tubes under water. After a further heat treatment at 1050°C for 15 m. in purified argon the specimens were drop quenched into stirred iced brine. The average quench rate measured with a chrome-alumel thermocouple attached to the specimens and having a bead diameter comparable with the specimen thickness, was 6000°C/sec. at the spinodal temperature (∿825°C). After this heat treatment the specimens had an average grain size of about 0.06 mm.

After aging in purified argon at the stated temperatures, the specimens were water quenched. Aging times were from 1 m. up to ∿1000 hours and all included about an additional 1 min. warm-up period. Because of this experimental limitation, aging times less than 1 min. could not be used. The aging temperatures were controlled to ±3°C.

2.2 Electron Microscopy

The strips were thinned initially to foils in a chemical polishing solution of 20 ml acetic acid, 10 ml nitric acid and 4 ml hydrochloric acid. Any surface deposit could be removed by immersion in this solution diluted

50/50 with water. Final electropolishing at 20 V potential was possible in a chromic-acetic acid solution (50 g CrO_3, 260 ml HAC and 8-10 ml H_2O) kept at ∿10°C. Some preferential polishing of one of the two phases always occured.

Foils were examined in a Siemens Elmiskop IA operated at 100kV. The magnification was calibrated by taking a series of photographs of a carbon grating of known spacing at different settings of the objective lens. The objective lens current measured with a digital voltmeter was then plotted against the true magnification to give a calibration curve for any particular setting of intermediate and projector lens currents. Micrographs were always taken using the same intermediate and projector lens settings and in this way the magnification could be determined to within 1% independently of stage position or specimen holder characteristics. If this check is not made, errors in magnification can be appreciable (20%) when using double tilting specimen devices.

Spinodal wavelengths were generally measured directly along a ⟨100⟩ direction on enlarged prints of micrographs taken in ⟨hk0⟩ orientation. The average wavelength and mean square deviation was calculated from a total of 100 measurements taken from at least five different areas. However, the most accurate mean value for the wavelength was obtained from measurements of side band spacings along ⟨100⟩ in the electron diffraction patterns, since these results do not depend on knowledge of the magnification. (See Table 1). Side bands in electron diffraction patterns have also been reported for Cu-Ti[15] and Alnico [16] alloys.

2.3 Magnetic Measurements

Curie temperatures were measured using equipment which has been described recently.[17] The specimen serves as the core between primary and

secondary circuits and output is obtained in the form of an induced voltage which is proportional to the magnetic permeability of the specimen. Normally, the absolute values of permeability are not important and the Curie temperature can be determined directly by following the change in induced voltage with temperature.

Specimens sized 3.5 cm x 6 mm x 0.3 mm were used and gave amplified induced voltages of the order of 0.5 V when ferromagnetic. The coil assembly was heated by placing it in a 2" diameter tube furnace fed with 60 V AC power. Temperature changes were measured with a thermocouple attached to the specimen and both thermocouple and induced voltage outputs were connected to strip recorders. The Curie temperature was the average value obtained from two separate heating and cooling cycles and the error in θc was $\pm 7^{\circ}C$. A specimen of pure annealed nickel was used to calibrate and check the performance of the apparatus.

2.4 Tensile Testing

Specimens were 8.5 mm x 0.3 mm with a 2.5 cm gauge length and were pulled to fracture in an Instron testing machine using a strain rate of .02 cm/min.

3. RESULTS

3-1 Microstructure

3-1.1 General Features. Figures 3 and 4 show the development of the spinodal microstructure which is coherent up to $\lambda \sim 1000\text{Å}$ (Fig. 3(b), 4(a-c) and then loses coherency by generation of interface dislocations (Fig. 4(d-f)). No evidence for transformation was obtained in fast quenched specimens either by microscopy (Fig. 3a) or by diffraction (i.e., no side band structure was observed, see Fig. 16a). The contrast which allows the two phase coherent microstructure to be distinguished results mainly from the differences in thickness and relative absorption between the copper rich and Ni/Fe rich phases. The copper rich phase is preferentially thinned during electropolishing and appears as the lighter colored regions, e.g., Fig. 4, 5, 9 etc. That these are the Cu rich regions is confirmed by comparison to Fig. 9 which is from alloy 2, viz. 70 Cu/21Ni/9Fe in which the Cu rich phase is the dominant one (volume fraction ~80%). Under dynamical diffraction conditions the interfaces show "δ-fringe contrast when inclined to the foil normal (e.g., Fig. 4(c), 10) because of the lattice parameter differences.[18] When loss of coherency occurs, the resulting dislocation structure is revealed under the usual diffraction conditions.

The interface plane is not rigidly confined to {100} even when the microstructure is coherent, as can be seen in some areas of Fig. 4(c). Imperfections in the periodicity of the spinodal structure are present at all stages and can be seen for example at A and B in Fig. 5. Even though the volume fraction is ~1/2, the microstructures do not appear to be continuous; the Ni/Fe rich phase seems to be embedded

in the copper rich phase.

Under the usual contrast conditions (viz., $\bar{g}.\bar{b} = 1$) matrix dislocations are not easily visible when the wavelength of the spinodal is of the same order as that of the dislocation image width (~100Å). Figure 6(a) shows three dislocations (arrowed) in a structure with $\lambda \sim 100$Å. The dislocations in Fig. 6(b) are imaged with a $\bar{g}.\bar{b}$ product of 3, and so appear wider than the dislocations in Fig. 6(a). Figures 6(b) and 6(c) show dislocations in alloy 1 aged at 775°C for 30 mins. ($\lambda \sim 300$Å) and 5 hours ($\lambda \sim 635$Å), respectively. The dislocations tend to lie along ⟨110⟩ in the {001} interfaces between the two phases and hence are mainly screws. These dislocations adopt a wavy shape when they cross the two phases (e.g., in Fig. 6(b) and at A in Fig. 6(c)).

Another important characteristic of the coherent spinodal is the absence of heterogeneous precipitate morphology so typical of many aluminum alloys, especially at grain boundaries. In fact, the absence of grain boundary recipitation and precipitate free zones is a good indication that decomposition is homogeneous (spinodal), This can be seen in Fig. 7 where grain boundaries cross the micrographs. The wavelength is ~150Å in Fig. 7(a) and 970Å in 7(b). Even in well coarsened structures such as Fig. 7(b), the two phases appear continuous right up to the boundary with no change in their spacing. However, grain boundary precipitation can be produced in these alloys by long aging treatments close to the spinodal temperature. Figures 8(a) (b) and (c) show optical micrographs of alloy 1 aged at 775°C for (a) 17 hours (b) 40 hours and (c) 500 hours. Grain boundary precipitation is barely discernible in (a), quite evident in (b) and almost a continuous grain boundary network in (c).

Figure 9 shows the microstructure of alloy 2 aged at 625°C for different times. Initially the microstructure consists of cubes with rounded corners which are not strongly aligned along the ⟨100⟩ directions, Fig. 9(a). Aging for longer times produces distinct alignment along ⟨100⟩ and a more pronounced cube morphology as in Fig. 9(b).

3.1.2. Loss of Coherency. Interfacial dislocations were not observed in alloy 1 aged at 625°C even after 940 hours when $\lambda \sim 1080$Å.

Interfacial dislocations in specimens aged at 700°C were first observed in a few areas after 40 hours. These dislocations occurred as single parallel sets lying in the interface along ⟨100⟩, as shown in Fig. 10. Contrast experiments using a variety of reflections showed that the most probable Burgers vector of these interface dislocations is a/2⟨110⟩ (e.g., Figs. 4(d), 10,12). As aging is continued and λ increases, the number of dislocations increases but their spacing (~300Å) is roughly constant. During this stage the diffraction patterns show splitting[19] along the interface normal (Fig. 11), which proves that a transitional tetragonal stage occurs as coherency is initially lost. Cubic symmetry is regained only when the interface network is completed by formation of the second set of dislocations (e.g., Figs. 12, 13). In Fig. 12(a) all of the dislocations are visible using the (002) and $(1\bar{1}\bar{1})$ reflections. Tilting so that g = (002) or $(1\bar{1}1)$ makes one set of the dislocations invisible. This is consistent with the network being composed of a/2 ⟨110⟩ dislocations of edge character with ⟨100⟩ long directions, although this example does not rule out the possibility that one set of the dislocations has $\bar{b}$ = a⟨100⟩.

Figures 13 and 14 show examples of the microstructure after cubic symmetry has been regained. The dislocation network in Fig. 13 has one

set of dislocations out of contrast with the $(11\bar{1})$ reflection operating. In Fig. 14 a definite change of habit plane from {100} towards {110} has occurred, as can be seen from the trace analysis. However, in many other areas the interface was still {100} or had become completely irregular as in Fig. 4(f). On many occasions curved dislocations were observed joining one dislocation network to another and passing through one of the phases. Several examples are arrowed in Fig. 14. The similarity between this two phase partially coherent microstructure to a well recovered single crystal single phase structure is remarkable.

3.1.3. Effect of Deformation. Foils prepared from specimens that had been deformed showed that slip dislocations generally sheared through the two phases. In deformed specimens with coherent phases, bands along ⟨110⟩ containing a high dislocation density were observed, which separated regions that were relatively dislocation free. In Fig. 15(a) many of the dislocations produced during deformation appear to lie along the interface between the two phases, e.g. at A while other dislocations appear curved.

Observations with thin foils of deformed specimens which were losing coherency showed that the interfacial dislocations did not take part in the slip process, but there was evidence for some interaction with the slip dislocations. Examples of interactions are arrowed in Fig. 15(b).

3.2 Measurement of Wavelength

Diffraction patterns taken of decomposed structures with $\lambda \lesssim \sim 150$Å exhibited satellite reflections (or so called side bands) along ⟨100⟩. Examples are shown in Fig. 16. The side bands spots are distinguished from the "split" spots due to transformation to tetragonality (Fig. 11) since the spacings of the side bands depend only on λ and not on Bragg angle along ⟨100⟩.

In Fig. 16(a) no satellite reflections are present in the quenched alloy while in Fig. 16(e) second order satellites are resolved at (400). The satellite spacing decreases gradually with aging time until the satellites cannot be distinguished from the main reflection.

The wavelength was calculated using the relationship[6]

$$\lambda = \frac{h \tan \theta \, a}{(h^2 + k^2 + l^2)\delta\theta}$$

where θ is the Bragg angle for the (hkl) reflection in a crystal of lattice parameter a, and $\delta\theta$ is the angular spacing between sideband and main reflection. For the (400) reflection and using a = 3.58Å this reduces to

$$\lambda = 0.89 \frac{r}{\Delta r}$$

where r and Δr are the distances from (000) and satellite to the (400) reflection. In the table below values obtained by this method from Fig. 16 are compared with the wavelengths measured from numerous micrographs similar to those of Fig. 3(b), 4(a-c). The results are in good agreement.

Table 1. Measurements of spinodal wavelengths

Aged at 625°C	from side bands in diffraction patterns *	from micrographs **
1 m.	61 ± 2	60 ± 6
5 m.	82 ± 3	95 ± 10
15 m.	110 ± 5	110 ± 14
60 m.	163 ± 5	150 ± 14

* Independent of magnification errors due only to measurement.
** Depends on magnification, precision of defining interface.

For $\lambda \gtrsim 150$Å the satellite spacing could not be used and measurements were taken directly from enlarged prints. The mean square deviation was calculated for each value of λ and was typically ±6 at $\lambda = 60$Å and ±75 at $\lambda = 667$Å.

Measurements from specimens which were losing coherency gave two different values for the wavelength. For example, in specimens of alloy 1 aged for 17 hours at 775°C there were some areas with $\lambda \sim 970$Å which were still fully coherent and contained no interfacial dislocations, e.g., Fig. 7(b). However, in the other areas where interfacial dislocations were present, the wavelength was measured as ~1850Å.

It was found that the variation of wavelength with aging time for coherent phases at the three temperature considered could best be expressed by the relationship $\lambda \propto kt^{1/3}$ as is shown in Fig. 17. Evaluation of the rate constant, k, for the three temperatures enabled an activation energy for growth to be calculated. A plot of log k^3 v 1/T gave a straight line whose slope corresponded to an activation energy of ~50 kcal/mole.

3.3 Measurement of Curie Temperature and Mechanical Properties

Typical results obtained from the magnetic analysis apparatus are shown in Fig.18. Curve (a) shows the variation of induced voltage with temperature for a quenched specimen of alloy 1; θ_c is obtained by extrapolation as ~237°C. The curve obtained from a specimen of pure nickel is plotted for comparison and gave $\theta_c \sim 358$°C. Curves (b), (c) and (d) illustrate the rapid change that occurs in θ_c as the alloy is aged at 625°C. Within 1 m. at 625°C [curve (b)] θ_c has increased to ~454°C, but changes only slightly with further aging for 15 m [curve (c)] and 5 hours [curve (d)]. The corresponding compositions of the Ni/Fe-rich regions can be found directly from the variation of Curie temperature plotted in

Fig. 2. It can be seen that over 80% change in composition has occurred after 1 min. and the structure consists of Ni/Fe rich regions containing ~20 at.% Cu.

The 0.1% yield stress of alloy 1 after quenching was ~10 kg/mm^2, and increased rapidly on aging reaching ~35 kg/mm^2 after 200 hours at 625°C and ~25 kg/mm^2 after 200 hours at 775°C. Elongation values for decomposed alloys were in the range 7-10% and fractures were predominantly intergranular. During aging the work hardening rate measured at 2% strain increased from ~120 kg/mm^2 in the quenched alloy to ~180-190 kg/mm^2 and remained approximately constant throughout the aging sequence, i.e., independently of whether the phases were coherent or semi-coherent.

Figures 19 and 20 summarize the changes that occur in yield stress, Curie temperature and wavelength for alloy 1 aged at 625°C and 775°C. Comparison to Fig. 2 shows that the compositions (as indicated by Curie temperatures) of the phases exceed that of the chemical spinodal limit within the first few minutes of aging. Beyond this the composition changes more slowly to approach the solvus limits corresponding to the tie lines at 625°C and 775°C. Thus, the compositions of the phases on attaining partial coherency (λ ~1000Å) lie outside the spinodal region indicated in Fig. 2. The plot of log ($\lambda - \lambda_o$) v. log aging time has a slope of 1/3 as expected from the results of Fig. 17. λ_o is the wavelength at zero time.

4. DISCUSSION

4.1 Partial Coherency

Matrix dislocations in the spinodal are confined to the interface over much of their length [as in Fig. 6(c)], and since the interface planes are {001} it is clear that only screw dislocations should be capable of this restriction and still remain glissile. The effect of forces due to internal stress and compositional gradients on dislocation behavior in spinodals has been discussed by Cahn.[20] He calculated that the stress field should cause alignment of the dislocations particularly at large compositional amplitudes or at long wavelengths. His calculations provide two convenient extremes for the dislocation behavior. If $\frac{A\eta\ bE}{\gamma\beta} < 1$ the dislocations should be almost straight while if this expression is > 1 the dislocations should be able to flex around the obstacles.

In this expression A is the amplitude of the compositional fluctuation, η is a parameter describing the compositional dependence of lattice parameter, E is Young's modulus, β is $2\pi/\lambda$ and γ is the self energy of the dislocation ($\sim Gb^2$).

For an alloy which has symmetrically decomposed, $A \sim \Delta c/2$, and using $G \sim 3E/8$ the above ratio reduces to $\sim 2\delta\lambda/3\pi\bar{b}$ where δ is the mismatch parameter which can be obtained from dislocation spacings using the well known Brooks formula, $\delta = \bar{b}/d$. In Fig. 6(c) $\delta \sim .006$, $\lambda \sim 635$Å and using $\bar{b} = 2.53$Å gives ~ 0.3 for this expression. Alignments of dislocations is thus observed at an earlier stage than Cahn predicts, although the evidence of Fig. 6(a) indicates that when the wavelength is small, alignment effects are not important.

There are two possibilities for the character of the interfacial dislocation if they have a/2 ⟨110⟩ Burgers vectors. For example, dis-

locations whose long direction is [100] in an (001) plane can be either pure edge with $\bar{b} = \pm a/2[0\bar{1}1]$ or $\pm a/2$ [011], or can be of mixed character with $\bar{b} \pm a/2$ [101] or $\pm a/2$ [$\bar{1}$01] at 45° to the dislocation line. The edge dislocation is expected to have the lowest overall energy and contribute most to the relief of mismathc. The mismatch direction is [001] for an (001) plane and so in any calculations the resolved edge component, $\bar{b}$ sine 45 must be used.

Dislocations of the form a⟨100⟩ may be expected for the most efficient relief of mismatch. This could then be achieved by half the number of dislocations if these were of the form a⟨100⟩rather than a/2 ⟨110⟩ with $\bar{b}$ at 45° to the mismatch direction. However, even if the nucleation of interfacial dislocations with such a large Burgers vector were energetically favorable, they are not expected to be stable in CuNiFe alloys because of the high anisotropy ratio.

The average dislocation spacing at A in Fig. 10 is ~200Å which when corrected for the 40-50° inclination of the habit plane at A gives a true spacing of ~280Å. Using the formula of Brooks, $\sigma = \bar{b}/d = \frac{\bar{b} \sin 45}{d}$ and assuming $\bar{b}_{(av)} = 2.53$Å gives $\sigma \sim 0.64\%$. The average dislocation spacing near the top of Fig. 4(d) and (e) was measured as ~300Å, giving $\sigma \sim 0.60\%$. This value of mismatch was checked from the [001] diffraction pattern shown in Fig. 11. Measurement of the split in (440) reflection gave $\sigma \sim 0.79\%$. For an alloy whose composition was close to that of alloy 1, Hargreaves[7] reported $\sigma \sim 1\%$ from his x-ray work after aging at 800°C for 24 hours. An interesting result is that loss of coherency occurs first by the generation of parallel dislocations to relieve mismatch but with the Burgers vectors at 45° to the mismatch direction (Fig. 10). In such an event, the structure must become tetragonal (at least locally) in one (or both) of the phases. This was proved to be the case by the

diffraction patterns, e.g., Fig. 11. A return to cubic symmetry occurs only when a second set of dislocations is created to relieve the mismatch completely.

Figure 11 was taken using selected area diffraction over a small region in the foil containing just one set of (010) interfaces. The direction of splitting is perpendicular to these habit planes, i.e., is along the mismatch direction expected for cubic-tetragonal interfaces. There is no splitting in the [100] direction, so there is no mismatch in the plane of the interface. This result is in agreement with the X-ray work of Hargreaves[7] who detected tetragonality after 24 hrs. at 800°C in a 50 Cu-35 Ni-15 Fe alloy. As coarsening continues, the number of dislocations at the interface increases (although their spacing remains approximately constant) until eventually dislocation networks are developed (Figs. 12-14). These networks are orthogonal with the long direction of the dislocations generally in ⟨100⟩ although there are some deviations from this as the interface rotates or becomes irregular. The networks are probably a result of the interactions of the a/2 ⟨110⟩ interfacial dislocations. For example, on the (001) plane, an a/2 [110] dislocation may be formed from the a/2 [011] and a/2 [10$\bar{1}$] of edge character that already exist. This resultant dislocation can have either an [010] or [100] long direction and so is of mixed character with its $\bar{b}$ in the plane of the interface. When the phases are cubic, there are three directions of mismatch, two in the interface plane and one along the plane normal. With a network of a/2 ⟨110⟩ dislocations, each $\bar{b}$ would make an angle of 45° to two of the three possible mismatch directions. This arrangement is expected to provide maximum relief of mismatch consistant with minimum overall energy. It appears likely, therefore, that the formation of such complete networks of interfacial dislocations is a result of the

transformation from tetragonal back to cubic structures. The x-ray work of Hargreaves confirms this suggestion, e.g., he found cubic phases after 240 hrs. at 800°C compared with the 200 hr. 775°C heat treatment considered in this analysis.

In summary, the phase transformations in this system may be written

$$\gamma_{fcc} \rightarrow \underset{\text{coherent}}{[\gamma_1 + \gamma_2]_{fcc}} \rightarrow \underset{\text{partial coherency}}{[\gamma_1 + \gamma_2]_{tetragonal}} \rightarrow \underset{\text{partial coherency}}{[\gamma_1 + \gamma_2]_{equil.\ cubic}}$$

Loss of coherency occurs around $\lambda \sim 950$Å during aging at 775°C and somewhere between 800-1350Å during 700°C aging. Aging at 625°C for 940h ($\lambda \sim 1080$Å) did not produce interfacial dislocations.

Possible mechanisms for the loss of coherency in several precipitate systems have been investigated by Weatherly and Nicholson.[23] They found that spherical precipitates of γ' in a Ni- base alloy and needle-shaped β' and S precipitates in Al-Mg-Si and Al-Cu-Mg alloys all lost coherency by the attraction of matrix dislocations to their interfaces. Weatherly and Nicholson also found that θ' plates in a Al-Cu alloy lost coherency by the nucleation and growth of small dislocation loops inside the precipitate. Another mechanism whereby precipitates can lose coherency which is independent of particle size and depends only on the mismatch exceeding a critical value is the punching of dislocation loops.[21] If loss of coherency depended on exceeding a critical value of mismatch in CuNiFe alloys then decomposition at 625° should produce loss of coherency before decomposition at 775°C because the mismatch between the two phases decreases with increasing temperature. However, the exact opposite of this is observed which is also in disagreement with the calculations of de Fontaine[22] which suggest that the maximum average wavelength before

coherency is lost should be inversely proporitonal to η the fractional change in lattice parameter per unit change in composition. For de Fontaine's calculations to agree with the observations made in this investigation, η must be larger at the higher aging temperature, and this cannot be the case.

Thus the mechanism involved the nucleation and growth of dislocation loops or the punching of dislocation loops, then the maximum wavelength attained before coherency is lost should be smaller at the lower aging temperature, which it is not. It seems probable that some interfacial dislocations must be spontaneously nucleated at the interface when the wavelength reaches a certain value. There will be an activation energy for this nucleation process which will be temperature dependent and this might explain why specimens aged at 775°C lost coherency at a shorter wavelength than at 625°C. Some support for this suggestion comes from the direct evidence for spontaneous nucleation of interface dislocations during growth obtained by Hren and Thomas[24] in Al-Ag alloys.

The absence of precipitation on dislocations or at grain boundaries is confirmation that nucleation is homogeneous as expected for an alloy within the spinodal. Grain boundary precipitation in alloy 1 aged at 775°C was however detected after ~ 17 hours (Fig. 8(a)) and after ~ 500 hours had developed into networks. This process is consequence of the growth of the phases that are adjacent to the boundary and coincides with the loss of coherency in the structure. Once coherency is lost, growth is no longer restricted to the {100} plane and phases located near the boundaries can coalesce. A possible reason for the accelerated rate adjacent to the boundary could be the easier nucleation or climb of the interfacial dislocations or enhanced grain boundary diffusion. Similar grain boundary precipitate has been observed in Au-Pt alloys by Tiedema et al[25].

4.2 Mode and Kinetics of Decomposition

The composition of alloy two is very close to the spinodal curve at 625°C[9] and alignment develops by selective growth . The connectivity of multiphase structures has been treated theoretically by Cahn.[26] He found that a high degree of connectivity is expected for phases whose volume fraction is greater than ~20% (alloy 1) whereas at volume fractions less than this isolated aggregates or holes of the minor phase should be formed (alloy 2). The change in morphology going from alloy 1 to alloy 2 (compare Fig. 9 with Figs. 4, 5, etc) is thus a consequence of the change in the relative volume fraction of the two phases. However, even in alloy 1 the structure appears to be that of the Ni/Fe phase embedded in a Cu-rich matrix rather than an idealized continuum.

Alloys of different composition along a tie-line decompose at any temperature to give structures differing only in the relative volume fraction of each phase. For alloy systems where the effect of coherency strains are small, the coherent spinodal and chemical spinodal will be in approximately the same position. The chemical spinodal curve can be calculated by the formula of Cook and Hilliard,[14]

$$c_s - c_c \sim (c_e - c_c)[1 - 0.422\ (T/T_c)]$$

where c_s and c_e are the spinodal and equilibrium compositions at temperature T, and c_c is the critical composition at the critical temperature T_c. Assuming the phases reach the equilibrium tie-line compositions the relative volume fractions of the 2 phases at the spinodal composition are

$$\frac{f_1}{f_1 + f_2} = \frac{c_e - c_s}{2(c_e - c_c)}$$

if the decomposition is symmetrical. Rearranging Cook and Hilliard's formula gives $f_1/f_1 + f_2 = 0.21\ T/T_c$, so with $T/T_c = 0.8$, $f_1/f_1 + f_2 \sim .17$

and as $T \rightarrow T_c$, $f_1/f_1 + f_2 \rightarrow .21$. Hence, the microstructure of alloys located inside the spinodal should consist of decomposed phases with volume fractions lying between .2 and .8. Isolated particles which align by selective growth are expected in decomposed structures with compositions either outside or lying close to the spinodal curve. As the alloy composition enters the spinodal the relative volume fraction increases and the critical size for alignment should decrease.[27] The structure should be rod or plate like and become more and more interconnected. For alloy compositions outside the spinodal, preferential nucleation on dislocations[3] or on other defects is expected because the free energy for nucleation is not zero in this region.

The values of wavelength reported by Hillert et al.[9] are in good agreement with those obtained in this paper. Hillert et al. found from x-ray diffraction that λ was ~179Å for a 56 Cu-31 Ni-13 Fe alloy aged at 625°C for 1 hour, compared to $\lambda \sim 150$Å found in this investigation. The discrepancy is probably due to the fact that in Hillert's work the alloys were not quenched from the solution treatment temperature but were isothermally transformed. Decomposition would be expected before the aging temperature were reached as soon as the specimen temperature crossed the spinodal, resulting in structures with a slightly greater wavelength.

Initial detection of the side bands appears to depend largely on the x-ray technique used,[28] and so it is clear that x-rays along should not be used for measuring the wavelength in spinodals because decomposition can take place before the intensity of the side bands is sufficient for them to be observed.[25,28] A further limitation is that the side band spacing decreases with aging time as the wavelength grows, and even-

tually cannot be measured. The results on the correlation of loss of coherency and formation of interface dislocations with changes from cubic tetragonal symmetry are in agreement with the suggestions of Hargreaves.[7]

The kinetics of growth of the wavelength at the three temperatures studied obeys the law $\lambda \propto kt^{1/3}$, consistent with the theories of coarsening where large particles grow at the expense of small ones by a diffusion controlled mechanism. The theory of particle coarsening was developed by Lifshitz and Slyozov[29] and Wagner[30] for spheres spatially distributed at random coarsening at constant volume fraction in a fluid system, but has been shown to apply in several non-ideal solid systems. In the Fe-Cu system, Speich and Oriani[31] found that the deviation in shape and the internal stress fields of the Cu particles did not affect the validity of the theory and a $t^{1/3}$ law was obeyed. This was also found to be the case in Ni-Al alloys[3] where there are alignment effects due to the selective growth of the γ'. The activation energy for coarsening was found in this investigation to be ~50 kcal/mole. Hillert et al.[9] has calculated that an additional ~10 kcal/mole is necessary to take into account the temperature dependence of the free energy change. The resultant ~60 kcal/mole is then in agreement with the activation energy of diffusion of ~66 kcal/mole reported by Daniel and Lipson and Hillert et al.

The main driving force for the coarsening process is the reduction in interfacial energy. A distribution of wavelengths exists at all stages and by dissolution of smaller particles in selected areas, adjacent ones can grow. Growth is assisted by the presence of numerous discontinuities in the periodicity of the structure. These imperfections have been reported in Alnico alloys by de Vos[32] who noted that they give a visual impression

of dislocation lines. An increase in wavelength would thus result if these "dislocations" were to "climb". In Fig. 5 imperfections are visible at A and B where dissolution has occurred resulting in a thickening of the adjacent particles. The coarsening rate is accelerated as coherency is lost, (when the driving force is now largely elastic) but insufficient data is available to say whether or not the $t^{1/3}$ law still applies, but with just a different rate constant. An increase in rate constant might be produced by a modification of the interfacial energy due to the presence of the dislocations, or an entirely different process may exist controlled by the rate of climb of the dislocations.

The wavelength of the first transformation product can be calculated from spinodal theory and has been defined[33] as the wavelength which maximizes the ratio of the free energy change to diffusion distance. Hillert et al. extrapolated their data to zero time and found values of initial wavelength which were larger than their calculations predicted. Typically at T/T_c ~0.8 (corresponding to the 625°C aging temperature) they extrapolated λ_o as ~93Å against a predicted λ_o of ~43Å for a 56 Cu-31 Ni-13 Fe alloy. When extrapolated, the coarsening plot from alloy 1 shown in Fig. 17 indicates that the initial wavelengths are about 30 to 35Å.

The results of the magnetic measurements show that the composition changes in the CuNiFe spinodal occur at a rapid rate, with about 82% of the composition changes taking place within 1 min. at 625°C, and about 98% change after 1 hour at 625°C. The changes in θ_c can be accurately related to the changes in composition by Fig. 2, where a ±7°C error in the measurement of θ_c reflects a change of only ±1 at.% Cu along the tie-line. From Fig. 2 the equilibrium compositions at 625°C and 775°C should have Curie temperature of ~508°C and ~435°C respectively, which are in

good agreement with the measured values. The Curie temperatures are sharp and hence correspond to a unique composition of the Ni/Fe rich phase after any particular heat treatment. This evidence indicates that the composition fluctuations are best expressed by a square rather than sine wave as indicated by the micrographs and side band patterns. This conclusion was also reached by Nagarajan and Flinn[34] who used Mössbauer spectroscopy to detect early changes in composition when CuNiFe alloys were aged. They also found an initial rapid increase in the volume fraction of non-magnetic (Cu-rich) phase by this technique. It appears likely, therefore, that the volume fraction of the two phases changes in a similar manner to the composition, becoming approximately constant after an initially sharp increase.

4.3 Age Hardening

The low yield stress of the quenched alloy is additional evidence together with the results of Figs. 3(a) and 16(a) that decomposition has not occurred during the quench. The majority of the dislocations in deformed specimens with coherent microstructures appeared in dense bands. Some of the dislocations were aligned along the interface, while others flexed around the interfaces. The decomposed structures is highly interconnected, and slip dislocations have no choice but to shear through both phases, producing no noticeable change in work hardening rate when the structure becomes partially coherent. Deformation of microstructures which contained interfacial dislocations again showed signs of shearing with the interfacial dislocations playing no part in the slip process. The interaction between slip and interfacial dislocations is a minor effect and for any particular slip system probably only exists for certain orientations of the particles.

Figures 19 and 20 summarize the results and allow the following conclusions to be drawn:

(1) The yield stress can increase with increasing wavelength at approximately constant Curie temperature, e.g., 2-5 m. 775°C, 40-200 h. 625°C.

(2) The yield stress is approximately constant even after the onset of partial coherency although the wavelength is still increasing, e.g., 40 h 775°C.

These conclusions do not suggest a simple relationship between yield stress, wavelength and Curie temperature (composition). Using λ and θ_c as parameters, various relationships were tried to explain the variation in yield stress but none were very successful. The most satisfactory results were obtained by a plot of yield stress v. Curie temperature, shown in Fig. 21 which gave a straight line through most of the data but with some deviations, noticeably at small wavelengths. A straight line could also be drawn just through the 625°C points in Fig. 21, but the majority of the data would then not be in agreement with such a plot. To a first approximation the yield stress is thus proportional to the amplitude of the composition fluctuations, A. However, this result is still not conclusive since changes in composition will produce changes in both lattice parameter and shear modulus of the two phases, and either (or both) of these parameters may control the hardening mechanism.

Any theory proposed to explain the age hardening mechanism in CuNiFe alloys must apply at both the aging temperatures studied and should be capable of predicting approximately correct values of yield stress for other spinodals such as Au-Pt.[35] The theories that have been proposed and can apply to spinodal systems[20,35-40] have been considered using λ and θ_c as varying parameters and bearing in mind the conclusions of the previous section. In order to test the theories the

assumption was made that the composition changes deduced from the measurement of θ_c were faithfully reflected as a difference in lattice parameter or shear modulus between the two phases. Estimated values of the maximum possible difference in these two parameters in the CuNiFe and AuPt systems which were used for analysis are listed in Table 2. These values have been calculated assuming the shear modulii and lattice parameters vary linearly with composition and the phases reach the equilibrium compositions estimated from the phase diagrams. The details of this appraisal are summarized in the appendix.

The theory which most closely agrees with experiment is that of Mott and Nabarro[36] in which the yield stress is determined by the internal stress fields. The theory was developed for structures containing a small volume fraction of spherical precipitates and so is not strictly applicable to alloy 1. However it predicts the observed yield stress and is supported by the direction observations of Fig. 6(b) and 6(c) and the linear dependence of yield stress with ϵ. One might expect the internal stresses to decrease when the tetragonal→cubic change occurs (~200 hrs. aging at 775°C, Fig. 20) so that on long overaging σ_i is expected to decrease. Unfortunately this cannot be tested experimentally because on such overaging drastic precipitation changes occur at the grain boundaries (Fig. 8(c)) so that the mechanical properties no longer depend on the spinodal characteristics.

5. SUMMARY AND CONCLUSIONS

The microstructure of the spinodal initially consists of rod-like blocks separated by diffuse interfaces which develop into distinct planer {100} interfaces as the wavelength enlarges. As the compositional amplitude and wavelength develop, matrix dislocations become restricted over much of their length to the interface between the two phases. Eventually coherency is lost and a/2 ⟨110⟩ interfacial dislocations of edge character with their Burgers vector at 45° to the mismatch direction are created. Finally, dislocation networks are produced and the habit plane becomes irregular and in place appears to rotate to {110}.

Coherency is lost during aging at 775°C when the wavelength reaches ~950Å. The maximum wavelength attained before interfacial dislocations are observed is greater at the lower aging temperature and suggests a temperature dependent nucleation process for the interfacial dislocations rather than a mechanism controlled by the mismatch parameter. The loss of cohrerency appears to occur in a two stage process--firstly, single parallel dislocation arrays are formed and the structure of the phases becomes tetragonal; secondly, a grid of dislocations is formed on long overaging and the structures become cubic again.

Associated with the loss of coherency is the observation of grain boundary precipitation which grows and eventually forms a complete grain boundary network.

In spinodal systems where the coherency strains are small, microstructures containing less than ~20% volume fraction of one of the phases are not expected to lie inside the spinodal. Such microstructures (as in

alloy 2) should consist of isolated cubes of the minor phase which align along ⟨100⟩ by selective growth.

The particles grow obeying the $\lambda = kt^{1/3}$ law developed for coarsening in a fluid system. The activation energy for coarsening is about 50 kcal/mole corresponding to that of matrix diffusion and in agreement with previous measurements. Coarsening depends on a distribution of wavelengths and their selective growth of dissolution. This is assisted by the by presence of numerous imperfections in the periodicity of the structure. As coherency is lost the coarsening rate is accelerated.

The initial composition fluctuations occur very rapidly and are best described by a square rather than a sine wave. They are large in amplitude (over 82% compositional change occurring within 1 min. at 625°C) but are on a small scale over regions ~20-30Å in size. As expected in a spinodal, nucleation is homogeneous with no evidence of heterogeneous precipitation on dislocations or grain boundaries. Coarsening takes place at approximately constant volume fraction with the phases slowly approaching and eventually reaching the equilibrium tie-line compositions.

During deformation of the spinodal most of the dislocations remain nearly straight and shear through the particles. In microstructures that are losing coherency the interaction between slip and interfacial dislocations is a minor one, and does not produce a noticeable change in the work hardening rate. The age hardening of the spinodal is controlled by the difference in lattice parameter of the two phases and is almost independent of the wavelength. Of the theories of the yield stress that can be used to explain the age hardening response in spinodals, the Mott-Nabarro theory of internal stresses in principle explains the present results and can account for the variation of yield stress in both the CuNiFe and the AuPt systems.

ACKNOWLEDGEMENTS

The author wishes to thank Dr. A. Goldberg of Lawrence Radiation Laboratory, Livermore for the loan of the magnetic coil assembly and Dr. M. F. Ashby for critical discussions, and is grateful to Professor G. Thomas for his advice and encouragement during this work. The research was supported by the U.S. Atomic Energy Commission through the Inorganic Materials Research Laboratory of the Lawrence Radiation Laboratory, Berkeley.

TABLE 2

Shear Modulus G $kg/mm^2 \times 10^3$

Cu	Ni	Fe	Au	Pt
5.56	9.67	8.8	3.23	6.37

Alloy	Heat Treatment	Measured yield stress kg/mm^2	Estimated composition and shear moduluii of 2 phases $kg/mm^2 \times 10^3$	Max ΔG $kg/mm^2 \times 10^3$	Max Δa (Å)	Calculated Δa (Å) $\Delta a = \delta . a$
51.5 Cu - 33.5 Ni 15.0 Fe	16h 625°C		11-56-33 $\bar{G}$ ~ 8.9			
	λ ~ 300Å	~35	81-17-2 $\bar{G}$ ~ 6.3	~2.6	~.045	~.030 (37)
average grain size ~.06 mm	40h 775°		24-49-27 $\bar{G}$ ~ 8.5			
a ~ 3.58Å	λ ~ 1330Å	~25	78-19-3 $\bar{G}$ ~ 6.4	~2.1	~.040	~.021 (section 4.1)
60 Au - 40 Pt*	510°C		2-98 $\bar{G}$ ~ 6.3			
average grain size ~.07 mm a ~ 4.02Å	λ ~ 160Å	~77	80-20 $\bar{G}$ ~ 3.9	~2.4	~.12	—

*Data for Au-Pt taken from Carpenters work (35).

APPENDIX

TESTS OF SPINODAL HARDENING THEORIES

Using the criteria developed in section 4.3 and the data of Table 2, the following summarizes the experimental tests of the various theories of spinodal hardening.

Mott and Nabarro (1940)

Mott and Nabarro[36] proposed that because of the difference in atomic volume that exists between two coherent phases there will be an internal stress field which will oppose dislocation motion. In a spinodal system this elastic strain field will have the same wavelength as the composition fluctuations and will produce alignment effects as observed and discussed in 4.1. As Cahn has pointed out,[20] cross-slip of the dislocations is of no use in avoiding these internal strains because the arrangement is identical on all {111}planes. For spherical precipitates, the theory predicts an average internal stress independent of particle size but dependent on the size factor between solute and solvent atom, ϵ, and the volume fraction of precipitating phase, f which is given by

$$\sigma_i \sim 2G\epsilon f$$

where G is the average shear modulus. If the elastic constants in the two phases do not differ appreciably and Poissons ratio is ~1/3, then $\epsilon \sim 2\delta/3$. Substituting $f \sim 1/2, \bar{G} \sim 7 \times 10^3$ kg/mm^2 and $\delta \sim \Delta a/a$ with a ~3.58Å gives $\sigma_i \sim 1.3 \times 10^3 \cdot \Delta a \sim 1.3 \times 10^3 (k\, \Delta\theta_c)$ where k is a proportionality factor. This predicted behavior is in agreement with the results of Figs. 19-21. Using the values of Δa given in Table 2 gives σ_i ~39 kg/mm^2 for the 625°C aging, and ~27 kg/mm^2 for the 775°C aging. These values are in very good agreement with the measured yield stress and

along with the evidence of Figs. 6(b) and 6(c) strongly suggest that the internal stress field controls dislocation motion in the spinodal.

The internal stress field can be estimated by measuring the radius of curvature of the dislocation, r, and using the formula

$$\sigma_i \sim G\bar{b}/2r$$

At point A in Fig. 6(c) r ~ 230Å, and using the values of G and $\bar{b}$ as before, then $\sigma_i \sim 38$ kg/mm^2 compared to the measured yield stress of the alloy after this heat treatment of ~ 25 kg/mm^2. The measured yield stress depends on the averaging out of forces that alternate in sign and is expected to be smaller than the actual internal stress maxima at any point.

The theory predicts a linear dependence of yield stress with changes in lattice parameter which is in agreement with the results of Fig. 21. However, the Mott-Nabarro theory also predicts a volume fraction dependence which was not found by Dahlgren[37] in this system. He reported that alloys with compositions along a tie-line aged at the same temperature had approximately the same yield stress even though the volume fraction varied from 0.25 to 0.50. Mott and Nabarro's theory was developed for a small volume fraction of spherical precipitates and the volume fraction dependence may not exist if f is large or if there is a change of morphology.

Fleischer (1960)

Fleischer[38] suggested that the image forces on a dislocation as it approaches a region in a crystal with a different elastic modulus may be large enough to make an important contribution to hardening. In a further paper[39] he derived a formula to estimate this effect and applied

his calculations to hardening due to thin zones in an Al - 2% Cu alloy. The stress on a screw dislocation a distance x from the precipitate interface is given by

$$t_{\Delta G} = \frac{\Delta G \bar{b}}{8\pi x} \left(\frac{a}{a+x}\right)$$

Where ΔG is the difference in shear modulus between matrix and precipitate, $\bar{b}$ is the Burgers vector of the dislocation and a is the thickness of precipitate measured along the slip plane. For {111} ⟨110⟩ slip in alloy 1 where f ~ 1/2, a ~ $\sqrt{3}\lambda/2$ and a reasonable value of x of ~ 2.5$\bar{b}$ has been suggested by Fleischer. Using these values and ΔG from Table 2 gives $t_{\Delta G}$ ~ 40 kg/mm^2 from the 625°C and ~ 33 kg/mm^2 from the 775°C data. By taking x ~ 3$\bar{b}$ values are obtained which are in agreement with the measured values, and if the changes in ΔG are proportional to changes in composition then the yield stress should be linear with θ_c in agreement with the results of Fig. 21. By suitable choice of the parameter x, the theory is also able to explain the apparent yield stress dependence on wavelength when λ is small, and the (a/a+x) term becomes important. The theory predicts the observed results of yield stress dependent soley on ΔG only when a is large compared to x.

However, there are two serious criticisms of Fleischer's theory which can be made. Firstly, the image forces on a dislocation increase as it approaches the interface and so alignment effects along the interface are not expected. Instead, matrix dislocations should lie preferentially in the phase where their overall energy is lowest. This would be the Cu-rich phase where the shear modulus is less than in the Ni/Fe rich phase although the required Burgers vector is slightly greater in the Cu-rich phase. Secondly, spinodal decomposition in the Au-Pt system produces

structures with yield stresses of the order of 70-80 kg/mm^2 and the theory does not appear able to explain such high values. Calculations of the maximum possible value of ΔG (Table 2) indicate that this is the same order of magnitude as in the CuNiFe system.

Cahn (1961)

Cahns theory of hardening by spinodal decomposition[20] has already been mentioned in 4.1. He calculated that the forces on dislocations due to the internal stress field were the most important and other forces such as due to the variation of energy of the dislocation with position or chemical hardening could be ignored. The theory predicts that for {111} ⟨110⟩ slip the applied stress necessary to move an edge dislocation will be given by:

$$\sigma_a^* = \frac{A^2\eta^2E^2b}{\sqrt{2}\beta\gamma}$$

Where the terms are defined in 4.1 η is defined as $1/a.\Delta a/\Delta c$ for small composition fluctuations, i.e. it is the same as the parameter ϵ used by Mott and Nabarro. For decomposition of an alloy in the center of miscibility gap $A \sim \Delta c/2$ and using the relationship $\delta \sim \Delta a/a$ gives $A\eta \sim \Delta c/2.1/a.\Delta a/\Delta c \sim \delta/2$. Assuming $E \sim 8G/3$ the applied stress reduces to

$$\sigma_a^* \sim \frac{8}{9\pi\sqrt{2}} \frac{\delta^2 G\lambda}{b} \sim 0.2 \frac{\delta^2 G\lambda}{b}$$

Using the 625°C data from Table 2, with $G \sim 7.6 \times 10^3$ kg/mm^2 gives $\sigma_a^* \sim 13$ kg/mm^2. Using the 775°C data and $G \sim 7.45 \times 10^3$ kg/mm^2 gives $\sigma_a^* \sim 28$ kg/mm^2.

The theory is thus only able to account for the measured yield stress when λ is large, and predicts a linear dependence of yield stress on $(\Delta\theta_c^2 . \lambda)$, which was not found. From Fig. 19 as λ increases from ~60Å

to ~ 600Å at approximately constant amplitude the measured yield stress increases by a factor of ~2 rather than a factor of 10.

Cahn also considered the case of dislocations able to curl around obstacles and slip through the opening between particles. This is the analogy of Orowan hardening and Cahn calculated that the stress for such a process depended on the reciprocal 2/3 power of the wavelength. The separation between particles is ~ $\lambda/2$ in a symmetrical alloy and using Cahn's formula the dislocation can slip through the opening if $\sigma_a > 4Gb/\lambda$. From the 775°C data with $\sigma_a \sim 25$ kg/mm^2, λ must be greater than ~ 3000Å for this process to occur. At such large wavelengths, coherency has been lost and the deformation characteristics of specimens are probably determined by the grain boundary precipitation.

Dahlgren (1966)

Dahlgren[37] investigated the yield stress of several CuNiFe alloys and concluded that the yield stress was proportional to the difference in lattice parameters of the two phases but appeared to be independent of volume fraction within certain limits and almost independent of wavelength. The results of the present investigation are generally in agreement with these conclusions, which also enable the higher yield stress in AuPt alloys to be satisfactorily explained if the mismatch is ~ twice that of CuNiFe, i.e. $\Delta a \sim .06$Å. This value of Δa is possible in the AuPt system (Table 2) where the coherency strains probably limit the phases from reaching the equilibrium tie-line compositions.

Ghista and Nix (1969)

Ghista and Nix[40] used a theoretical approach with a dislocation model to explain the strength of elastically inhomogeneous materials. The elastic energy of dislocations in such materials will vary with position

as the shear modulus fluctuates periodically. Assuming a sine wave fluctuation the theory predicts that the yield stress should $\propto \Delta G/\lambda$. Using selected values of these parameters, Ghista and Nix were able to explain the yield stress of a Au-Pt alloy after a particular heat treatment. The theory cannot go further than this, however, and it is incapable of explaining the yield stress or its variation in the CuNiFe system. A reciprocal relationship of yield stress with λ is not observed, and the estimated value of ΔG in both systems is about the same.

REFERENCES

1. J. W. Cahn, Trans. TMS-AIME, 242, 166 (1968).
2. A. H. Schultz and V. S. Stubican, Phil. Mag. 17, 929 (1968).
3. A. J. Ardell and R. B. Nicholson, Acta Met. 14, 1295 (1966).
4. K. B. Rundman and J. E. Hilliard, Acta. Met. 15 1025 (1967).
5. R. H. Redwine and M. B. Field, J. Mater. Sci. 3, 380 (1968).
6. V. Daniel and H. Lipson, Proc. Roy. Soc. 182, 378 (1943).
7. M. E. Hargreaves, Acta Cryst. 4, 301 (1951).
8. E. Biedermann and E. Kneller, Z. Metallk, 47, 289 (1956).
9. M. Hillert, M. Cohen and B. L. Averbach, Acta Met. 9, 536 (1961).
10. R. B. Nicholson and P. J. Tufton, Z. Angew. Physik, 21, 59 (1966).
11. R. K. Ham, J. S. Kirkaldy, and J. T. Plewes, Acta Met. 15, 861 (1967).
12. R. E. Villagrana, Ph.D. Thesis, University of California, Berkeley, UCRL Report No. 17345 (1967).
13. W. Köster and W. Dannöhl, Z. Metallk, 27, 220 (1935).
14. H. E. Cook and J. E. Hilliard, Trans. TMS-AIME 233, 142 (1965).
15. K. Saito and R. Watanabe, J. Phys. Soc., Japan 22, 681 (1967).
16. E. B. Granovsky, A. A. Fridman, P. P. Pashkov, and Ya. S. Umansky 4th Eurpean Regional Conference on Electron Microscopy, Rome p. 439 (1968).
17. A. Goldberg, W. U. Dent and J. H. Miller, J. Sci. Instrum, 44, 200 (1967).
18. R. Gevers, J. Van Landyt and S. Amelinckx, Phys. Stat. Sol. 11, 689 (1965).
19. G. Thomas, Trans TMS-AIME, 233, 1608 (1965).
20. J. W. Cahn, Acta Met. 11, 1275 (1963).

21. G. C. Weatherly, Phil. Mag. 17, 791 (1968).

22. D. de Fontaine, Acta Met. 17, 477 (1969).

23. G. C. Weatherly, and R. B. Nicholson, Phil. Mag. 17, 801 (1968).

24. J. A. Hren and G. Thomas, Trans TMS-AIME 227, 308 (1963).

25. T. J. Tiedema, J. Bouman and W. G. Burgers, Acta Met. 5, 310 (1957).

26. J. W. Cahn, Acta Met. 14, 477 (1966).

27. H. Gleiter and E. Hornbogen, Mater. Sci. Eng. 2, 285 (1968).

28. V. A. Phillips, Inst. of Metals (London) Report of Conference on "Mechanisms of Phase Transformations in Crystalline Solids," Manchester 1968.

29. I. M. Lifshitz and V. V. Slyozov, J. Phys. Chem. Solids 19, 35 (1961).

30. C. Wagner, Z. Electrochem. 65, 581 (1961).

31. G. R. Speich and R. A. Oriani, Trans. TMS-AIME 233, 623 (1965).

32. K. J. de Vos, J. Appl. Phys. 37, 1100 (1966).

33. M. Hillert, Acta Met. 9, 525 (1961).

34. A. Nagarajan and P. A. Flinn, Appld. Phys. Lett. 11, 120 (1967).

35. R. W. Carpenter, Acta Met. 15, 1297 (1967).

36. N. F. Mott and F. R. N. Nabarro, Proc. Phys. Soc. 52, 86 (1940).

37. S. D. Dahlgren, Ph.D. thesis, University of California, Berkeley, UCRL-16846, May 1966.

38. R. L. Fleischer, Acta Met. 8, 598 (1960).

39. R. L. Fleischer in "Electron Microscopy and Strength of Crystals," J. Wiley and Sons, New York, p. 973, (1963).

40. D. N. Ghista and W. D. Nix, Mater. Sci. Eng. 3, 293 (1969).

FIGURE CAPTIONS

Fig. 1 Ternary equilibrium diagram for the CuNiFe system showing the tie-lines with the 625°C and 775°C solvus lines (13) and the compositions of alloys 1 and 2.

Fig. 2 The pseudo binary section of the CuNiFe system used in this investigation. X and Y are the expected equilibrium tie-line compositions of the decomposed phases when alloy 1 is aged at 625°C.[13] The chemical spinodal was calculated using $T_c \sim 825°C$ and $c_c \sim 0.50$ from Ref. (14). The Curie temperatures of the quenched alloys were taken from Ref. (13) with the exception of the open circle corresponding to alloy 1.

Fig. 3 Transmission electron micrographs of alloy 1 (a) fast quenched showing no sign of decomposition, (b) aged 1 min 625°C showing very fine rod shaped particles ~ 30Å in size ($\lambda \sim 60$Å).

Fig. 4 Alloy 1 aged at 775°C for (a) 2 min, $\lambda \sim 150$Å, (b) 15 min., $\lambda \sim 254$Å, (c) 5 hrs. $\lambda \sim 635$Å, (d) 17 hrs. $\lambda \sim 970$Å, (e) 40 hrs. $\lambda \sim 1330$Å, (f) 200 hrs. $\lambda > 5000$Å. The microstructure initially consists of irregular rod-like particles separated by diffuse interfaces (a) which during coarsening develop distinct planar interfaces (c), and eventually lose coherency (d-f). Diffracting conditions are the same in all micrographs with $\bar{g} = (200)$ operating from left to right with foil orientations $\langle hk0 \rangle$.

Fig. 5 Imperfections in periodicity (at A and B for example) in alloy 1 aged 5 hrs. 775°C. The orientation of the foil is [110] with the (001) planes perpendicular to the foil surface.

Fig. 6 Matrix dislocations in alloy 1 (not deformed) aged (a) 2 m. 700°C ($\lambda \sim 100$Å) showing that the dislocations (arrowed) do not initially lie along the interfaces; (b) 30 min. 775°C ($\lambda \sim 300$Å) showing dislocations along $[1\bar{1}0]$ which are wavy as they cross the two phases (c) 5 hrs. 775°C ($\lambda \sim 635$Å) showing dislocations along $[1\bar{1}0]$ which are restricted over much of their length to the interface between the two phases, and are wavy when they cross regions containing alternating phases, eg at A.

Fig. 7 Grain boundaries in alloy 1 showing the absence of precipitation at the boundaries after aging for (a) 2m 775°C (b) 17 hrs. 775°C. Even in well coarsened but still coherent microstructures such as (b), there is no heterogeneous or grain boundary precipitation. Notice in (a) that the spinodal is still resolved under weak (kinematical) diffracting conditions (top grain).

Fig. 8 Optical micrographs of alloy 1 aged at 775°C for (a) 17 hours (b) 40 hours and (c) 500 hours showing that grain boundary precipitation is observed after long aging times and forms a grain boundary network. (x 800).

Fig. 9 The microstructure of alloy two aged at 625°C showing, (a) after 18 hrs, cubes with rounded corners which are not strongly aligned along $\langle 100 \rangle$, (b) after 300 hrs, alignment by selective growth has occurred.

Fig.10 Interfacial dislocations in alloy 1 aged for 200 hours at 700°C ($\lambda \sim 1355$Å) are visible when imaged with $\bar{g} = (1\bar{1}\bar{1})$ as in (a) and are invisible in (b) where $\bar{g} = (1\bar{1}1)$. The long direction of the dislocations is [001] and their most probable Burgers vector is a/2 [110]. Displacement fringes are also visible.

Fig. 11 Diffraction pattern of an [001] zone in alloy 1 aged 775°C 40 hrs showing the (400) (420) and (440) relfections. The resolvable split in the (440) reflection (arrowed) is along the interface normal and there is no splitting in the [100] direction, i.e. the alloy is tetragonal after this heat treatment.

Fig. 12 Dislocation networks developed by aging alloy 1 for 200 hours at 775°C. In (a) all three dislocations in the network are in contrast using both the $(1\bar{1}\bar{1})$ and (002) reflections, in (b) and (c) only two sets are in contrast using the $(1\bar{1}1)$ and (002) reflections.

Fig. 13 Dislocation network in alloy 1 aged for 200 hours at 775°C with one set of the dislocations invisible with $\bar{g} = (11\bar{1})$. The habit plane is irregular and does not analyse to be exactly {100}.

Fig. 14 Well developed networks of interfacial disolcations in alloy 1 aged for 200 hours at 775°C. One set of dislocations is invisible with $\bar{g} = (11\bar{1})$ and a rotation of the (001) habit plane to (011) has occurred (e.g. at the right hand side of the micrograph). Also visible are dislocations joining one network to another on the opposite side of the interface (arrowed). Foil normal [110].

Fig. 15 The microstructure of deformed specimens of alloy 1 after aging for (a) 940 hrs. 625°C and cold rolling 5% (b) 200 hrs. 700°C and pulled in tension 1.4%. Many of the dislocations in (a) are aligned along the interfaces (e.g. at A). Interfacial dislocations are visible in (b) at (I), slip dislocations at (S), and displacement fringe contrast at (F), with some interaction between the slip and interfacial dislocations (arrowed).

Fig. 16 Diffraction patterns of alloy 1 after quenching and aging at 625°C showing the origin, (200) and (400) reflections with the satellite reflections along [100]. (a) fast quenched (b) 1 m (c) 5 m (d) 15 m (e) 60 m. The satellite spacing decreases with aging times as the wavelength grows.

Fig. 17 Plot of wavelength v. (aging time)$^{1/3}$ determined for alloy 1 for the three temperatures studied.

Fig. 18 (A,B) Induced voltage v. temperature curves obtained from the magnetic analysis. Curve (a) is for alloy 1 fast quenched where $\theta_c \sim 237°C$ and the results obtained from the pure nickel specimen ($\theta_c \sim 358°C$) are plotted for comparison. Curves (b) (c) and (d) are for alloy 1 aged at 625°C for 1 m, 15 m, and 5 hours respectively.

Fig. 19 Summary of the changes that occur in yield stress, Curie temperature and wavelength as alloy 1 is aged at 625°C.

Fig. 20 Summary of the changes that occur in yield stress, Curie temperature and wavelength as alloy 1 is aged at 775°C. Coherency is initially lost after 17 hrs. when $\lambda \sim 1000Å$ and after 200 hrs. dislocation networks are formed.

Fig. 21 Plot of yield stress v. Curie temperature for alloy 1 fast quenched and then aged for different times at temperatures between 625°C and 825°C.

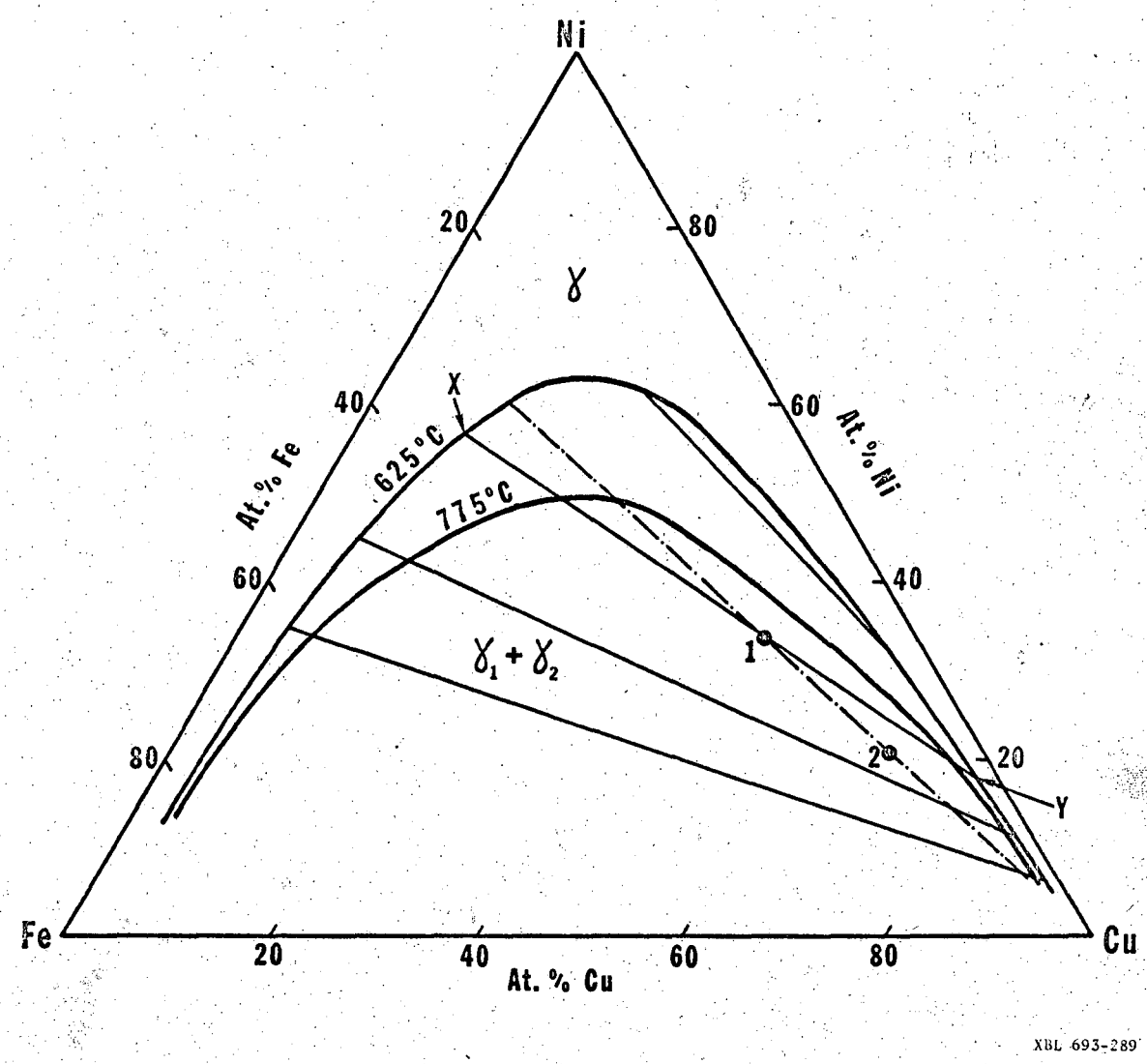

XBL 693-289

Fig. 1

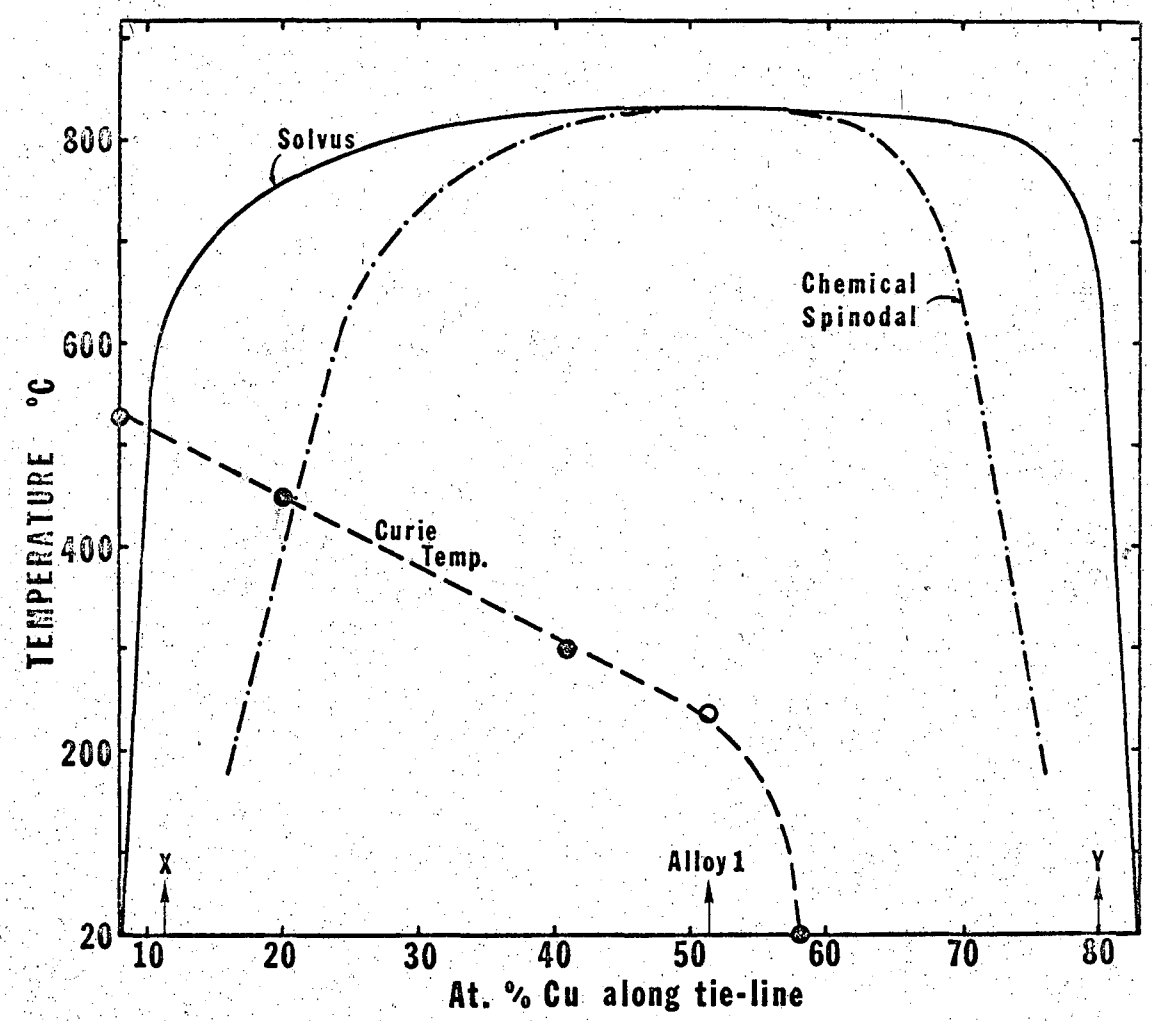

XBL 693-293

Fig. 2

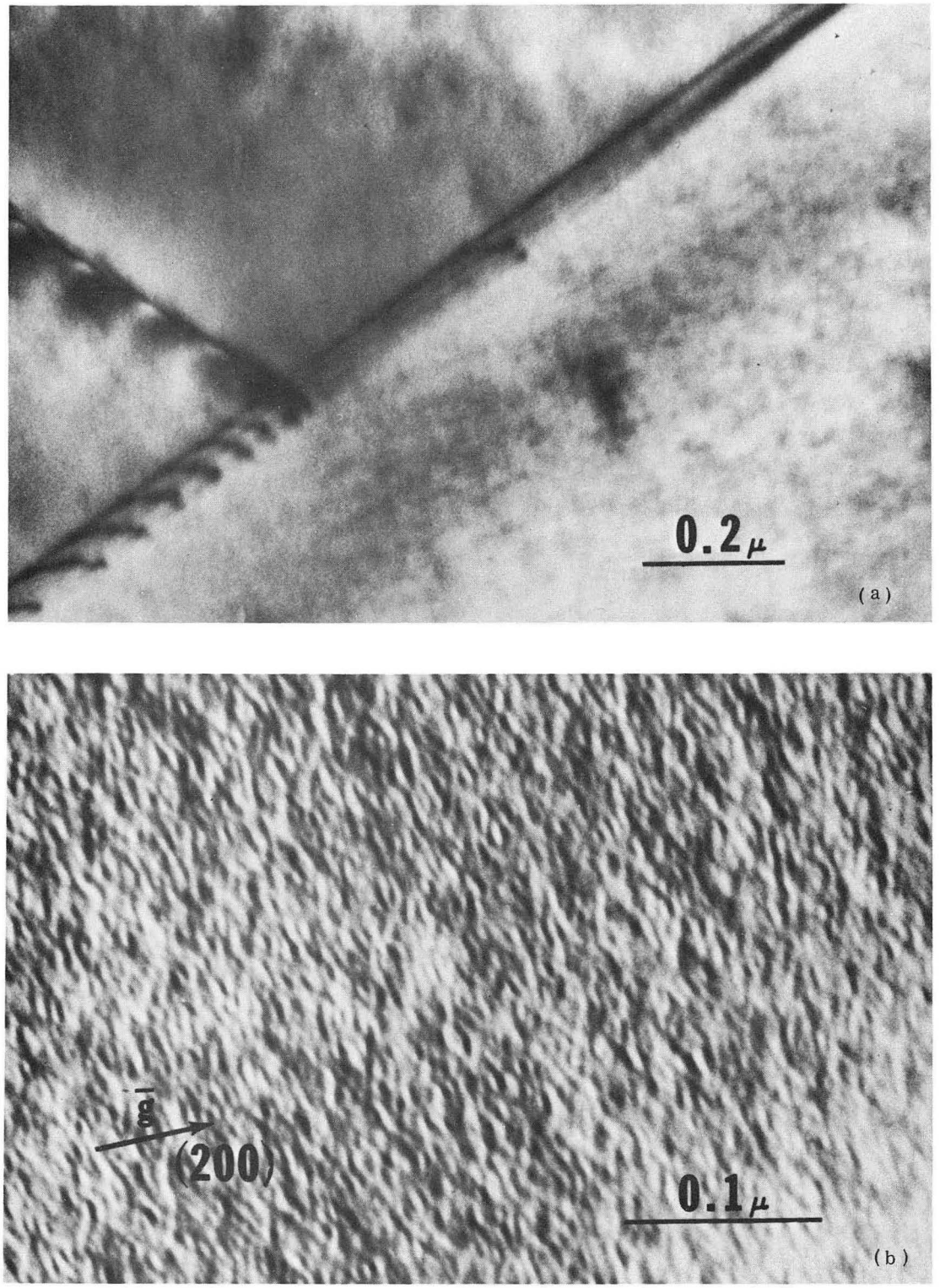

XBB 693-1862

Fig. 3

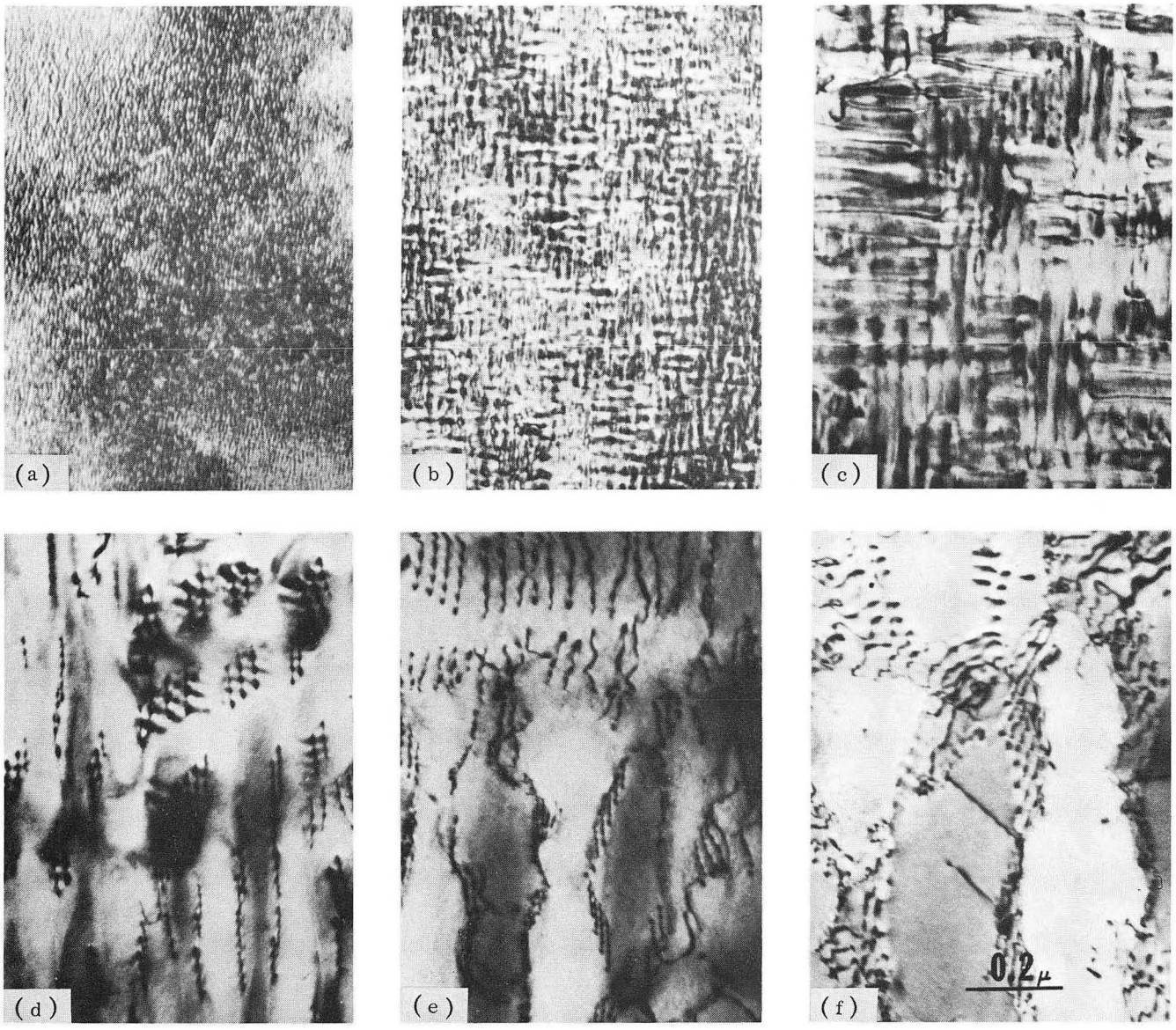

XBB 694-2456

Fig. 4

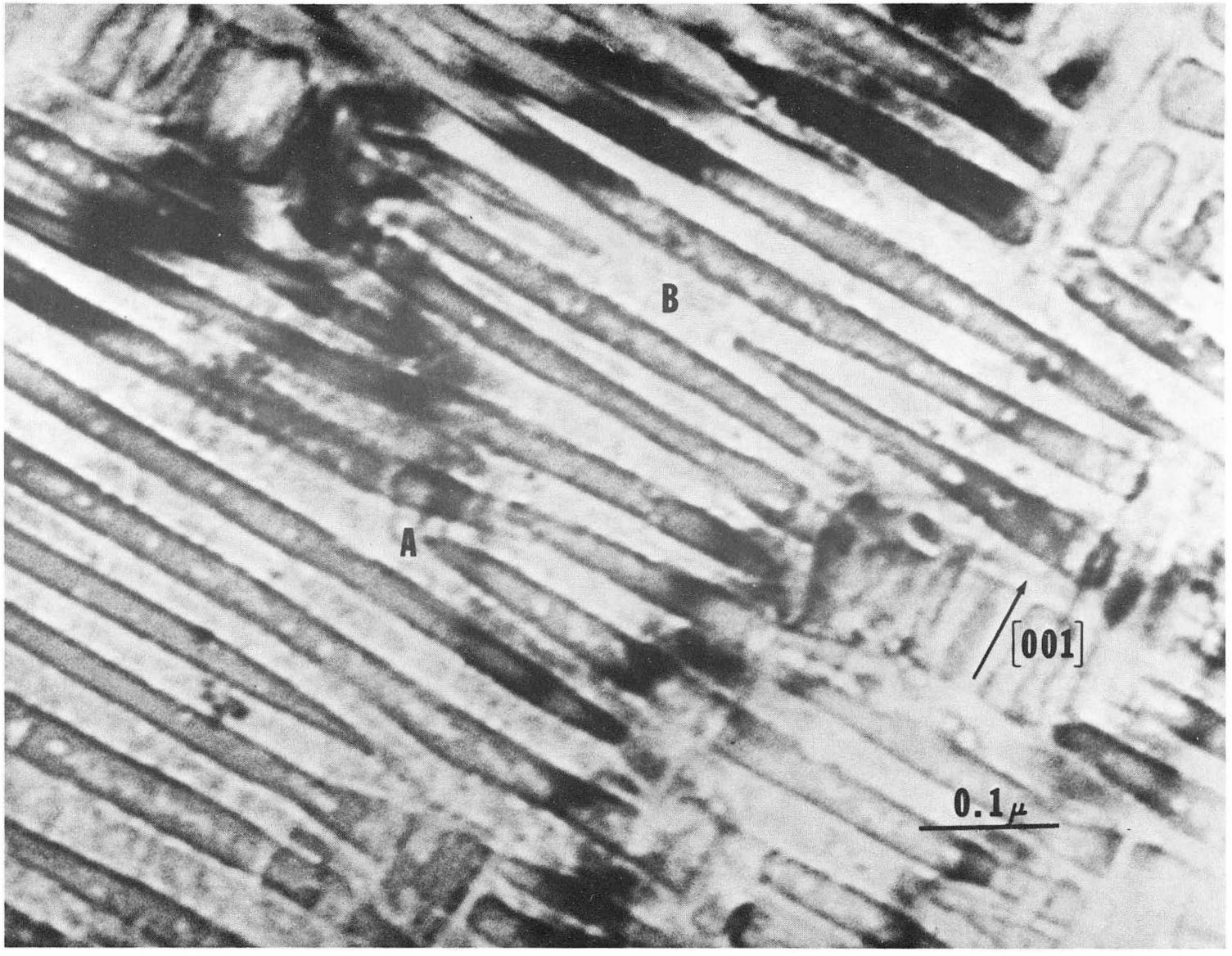

XBB 693-1869

Fig. 5

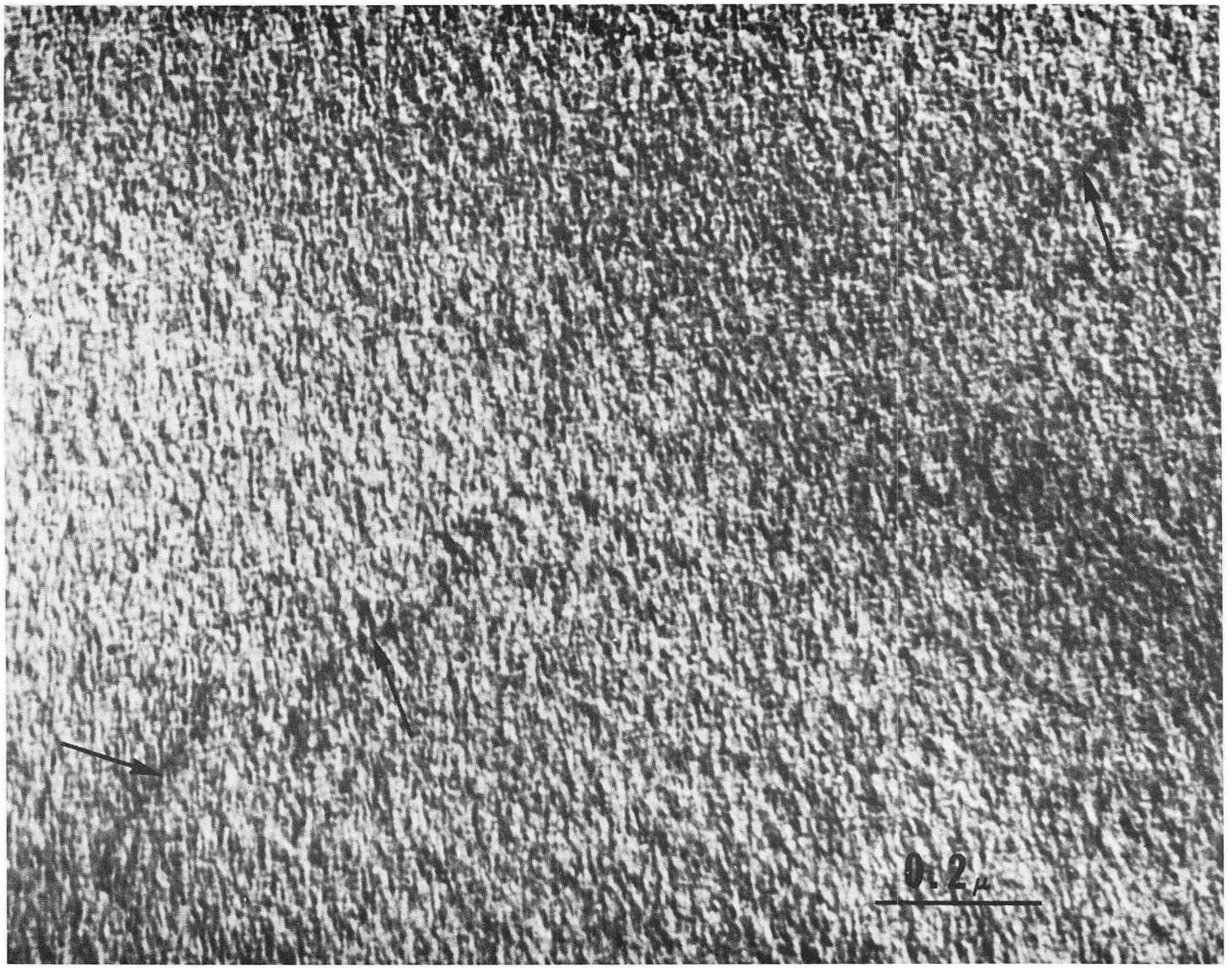

XBB 693-1868

Fig. 6(a)

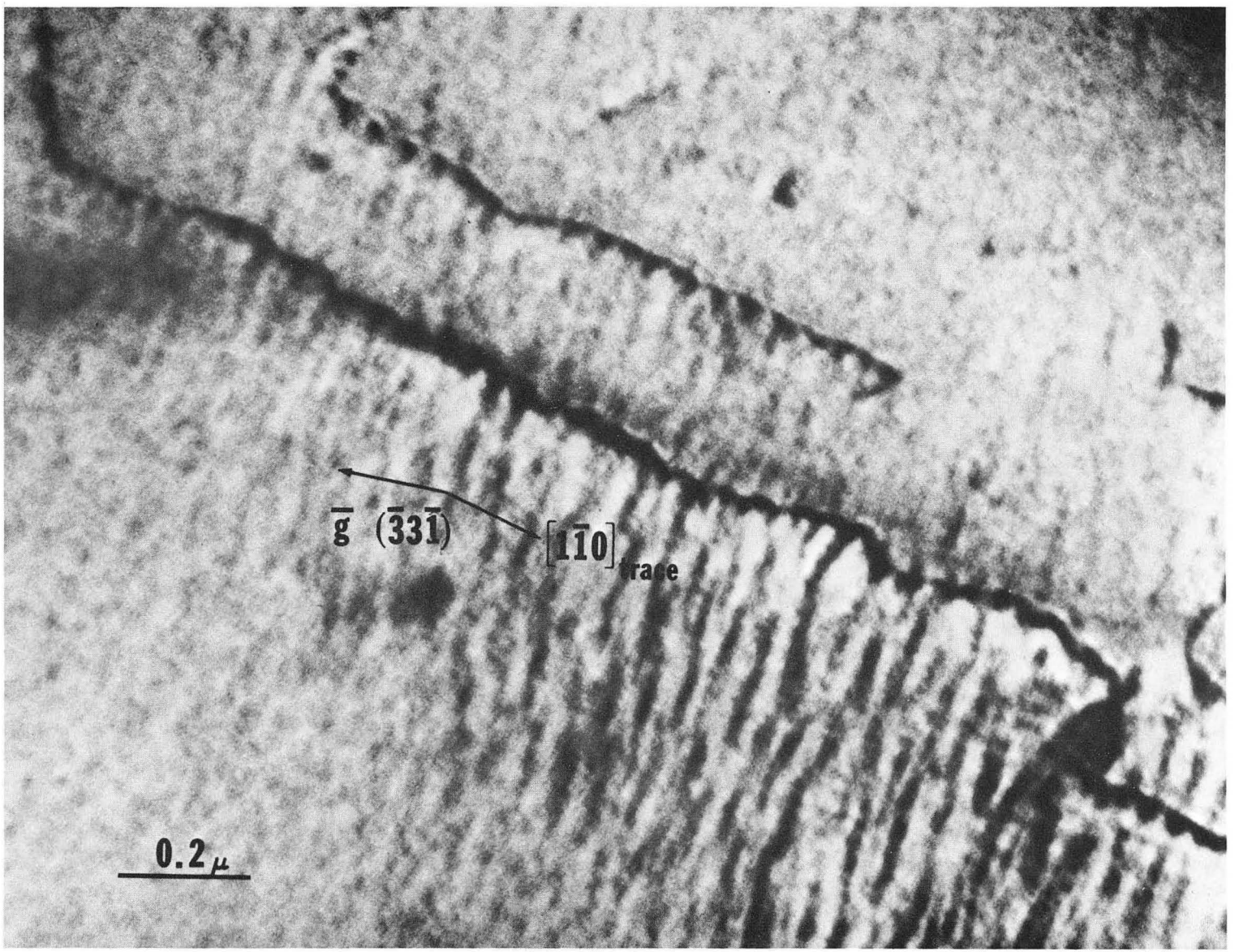

XBB 694-2663

Fig. 6(b)

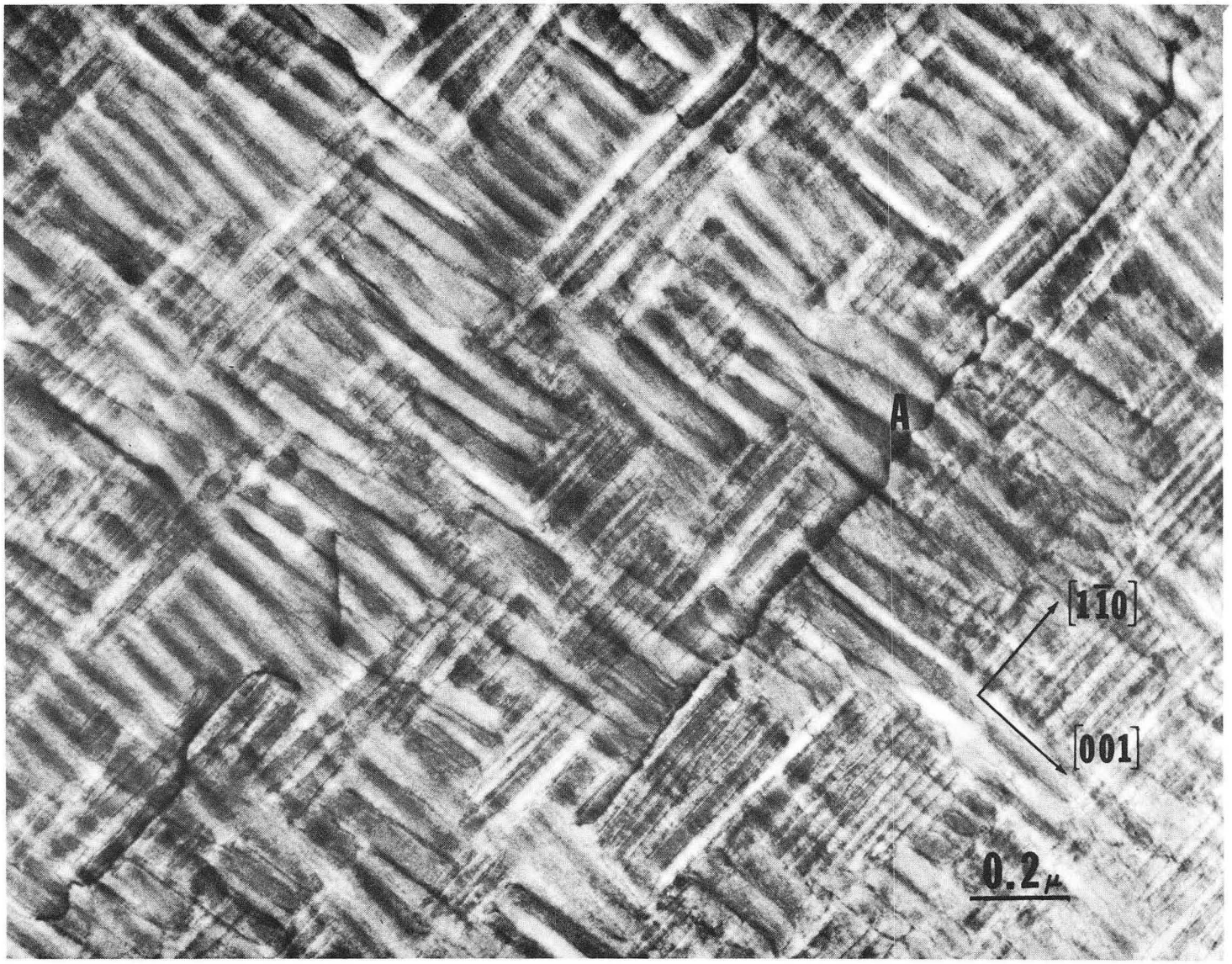

XBB 693-1871

Fig. 6(c)

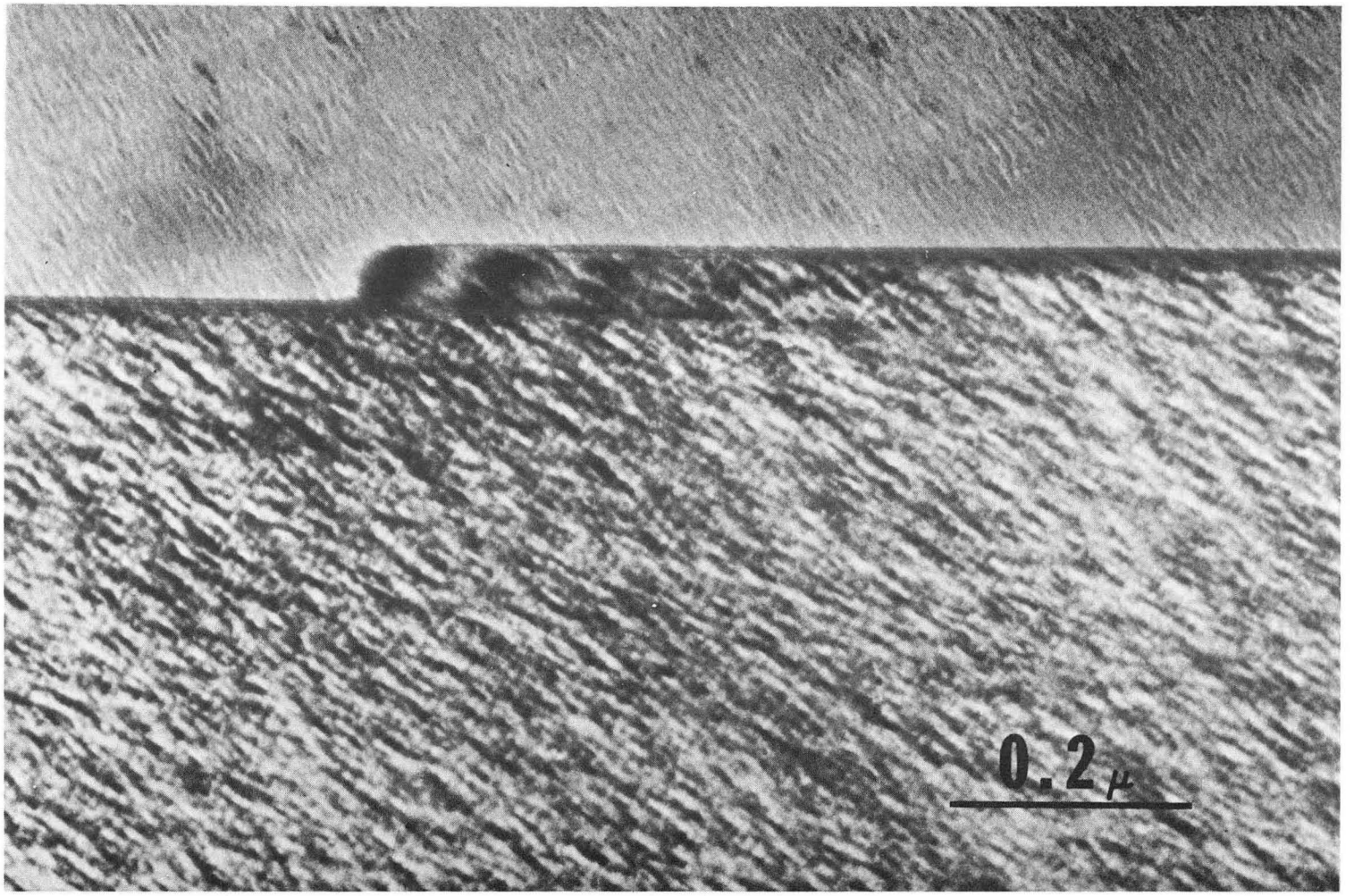

XBB 693-1863

Fig. 7(a)

XBB 691-243

Fig. 7(b)

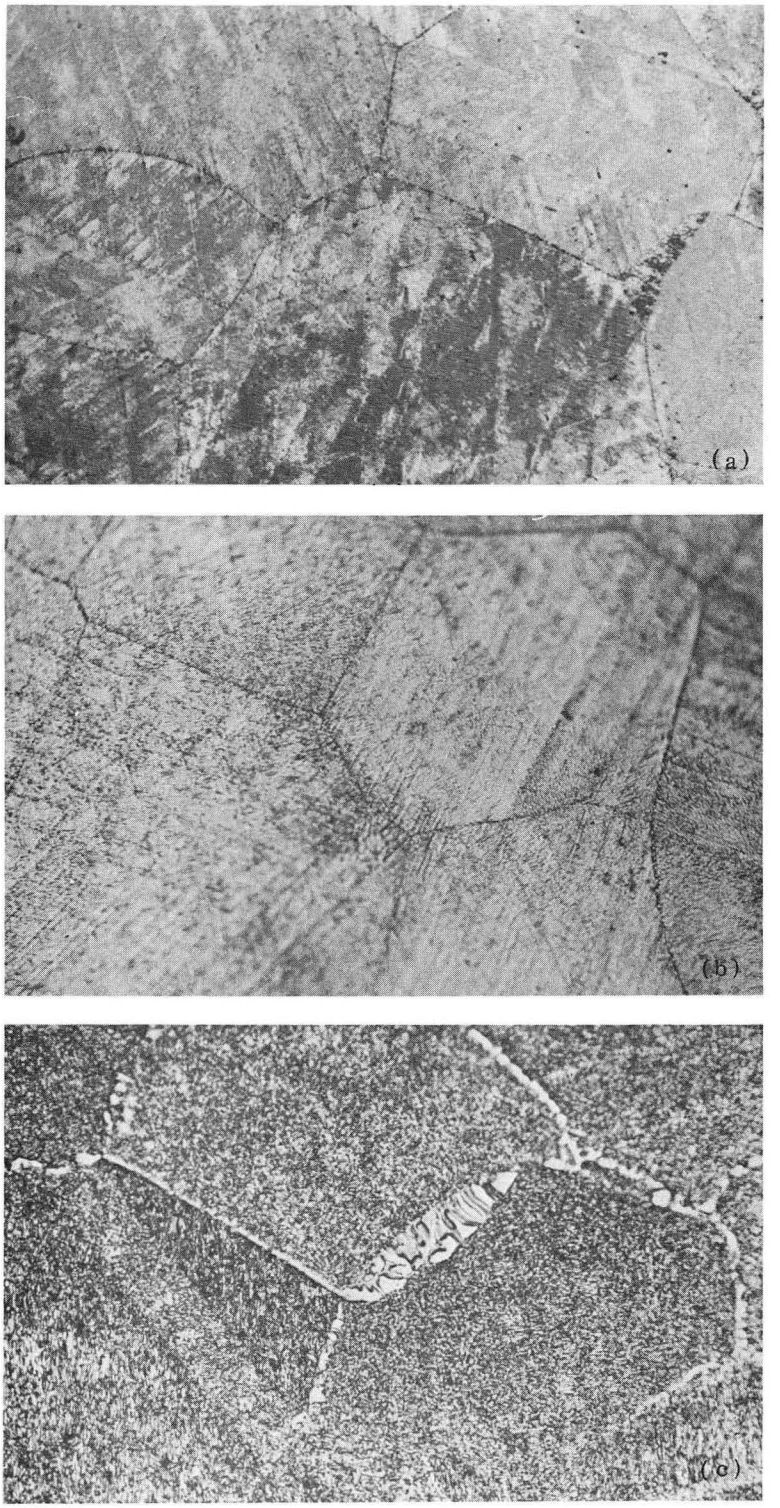

XBB 693-1858

Fig. 8

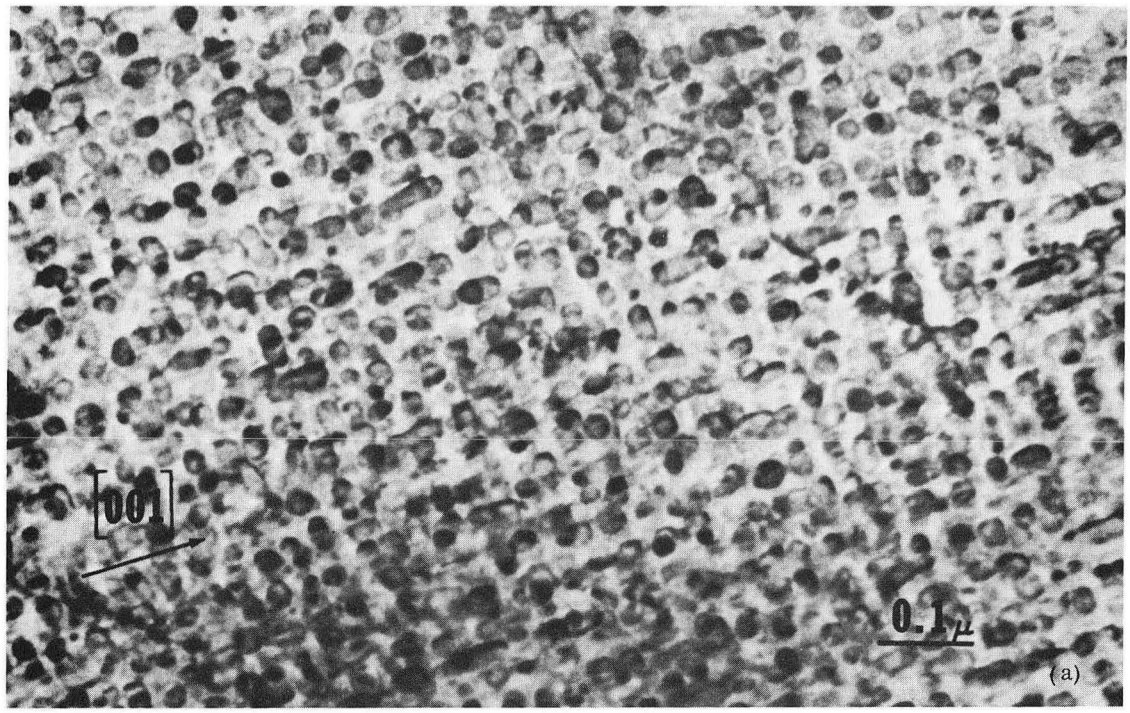

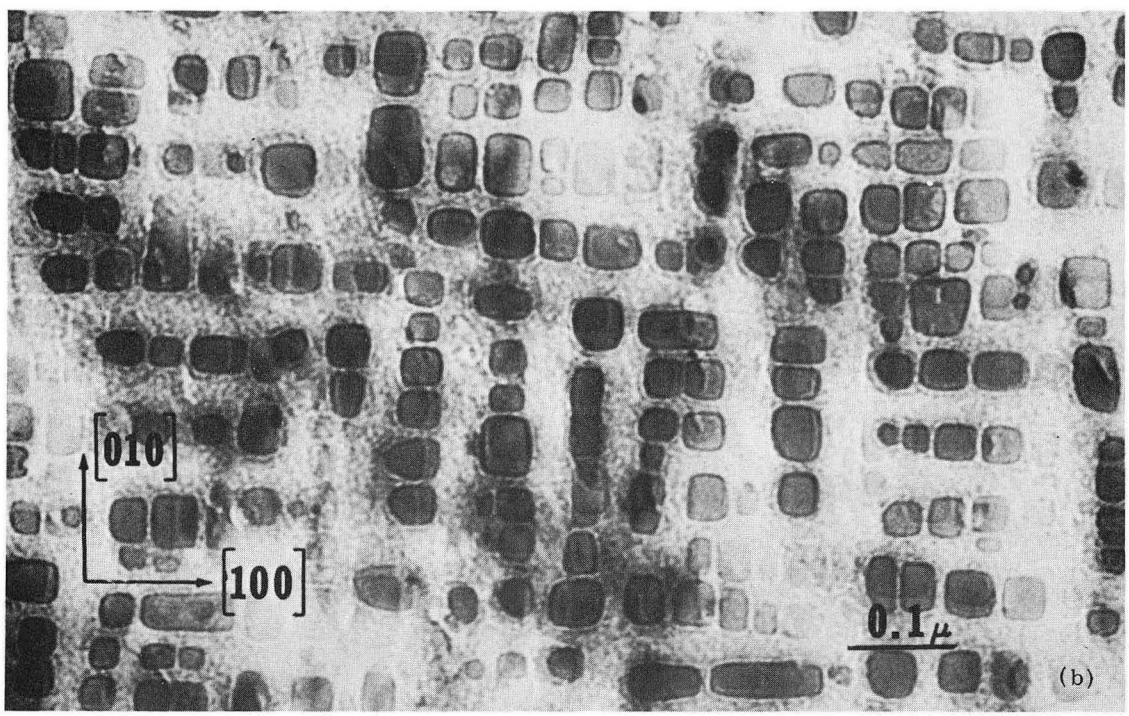

XBB 693-1864

Fig. 9

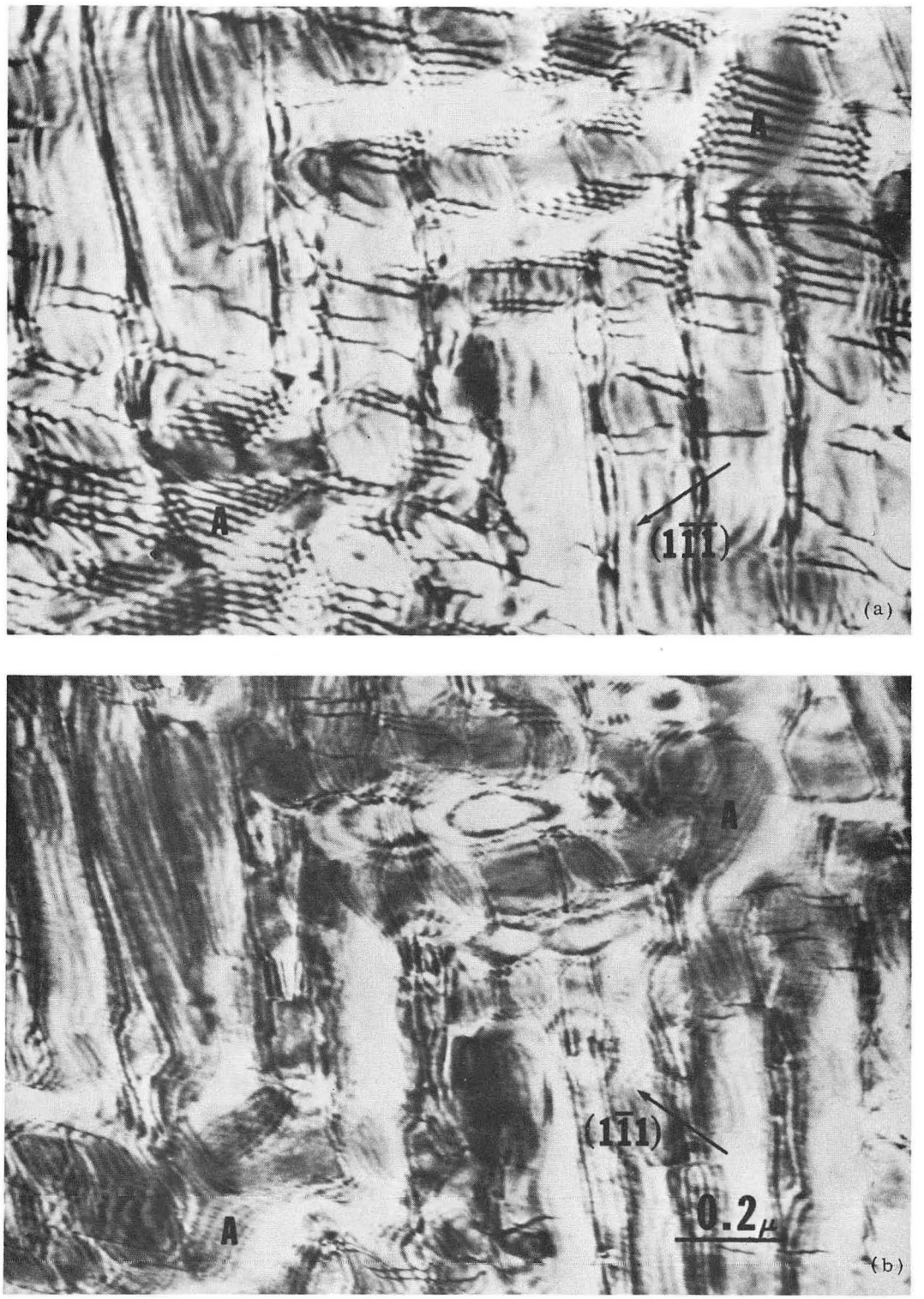

XBB 693-1861

Fig. 10

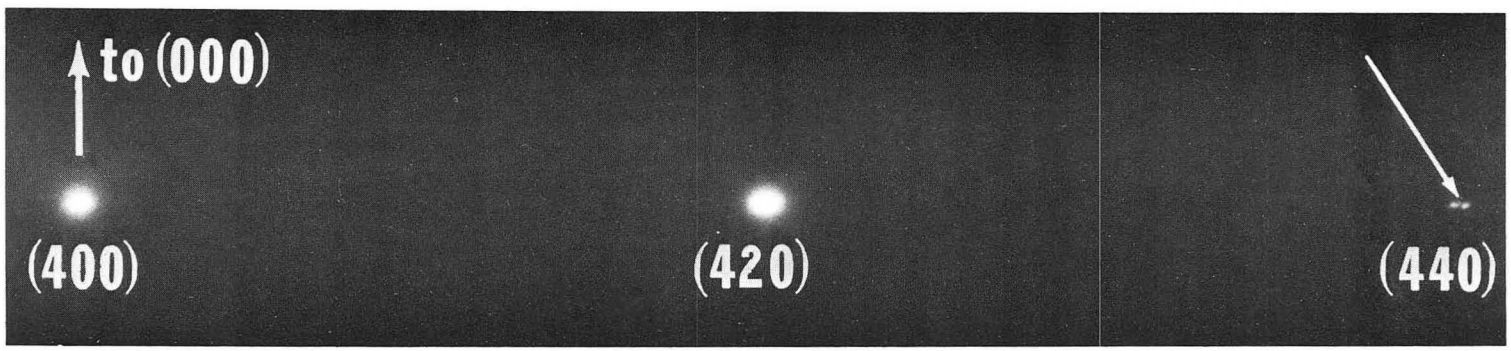

XBB 694-2455

Fig. 11

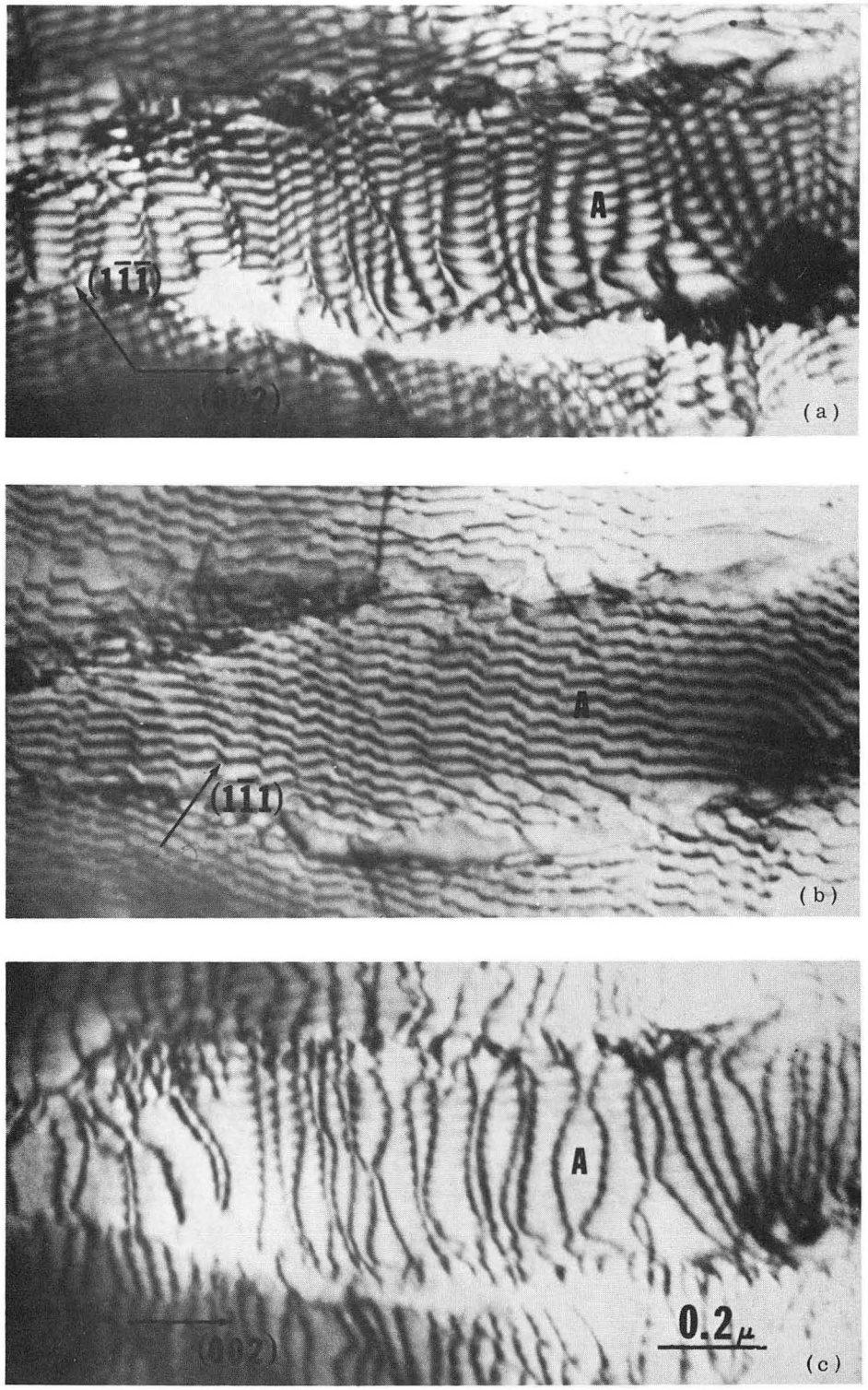

XBB 693-1860

Fig. 12

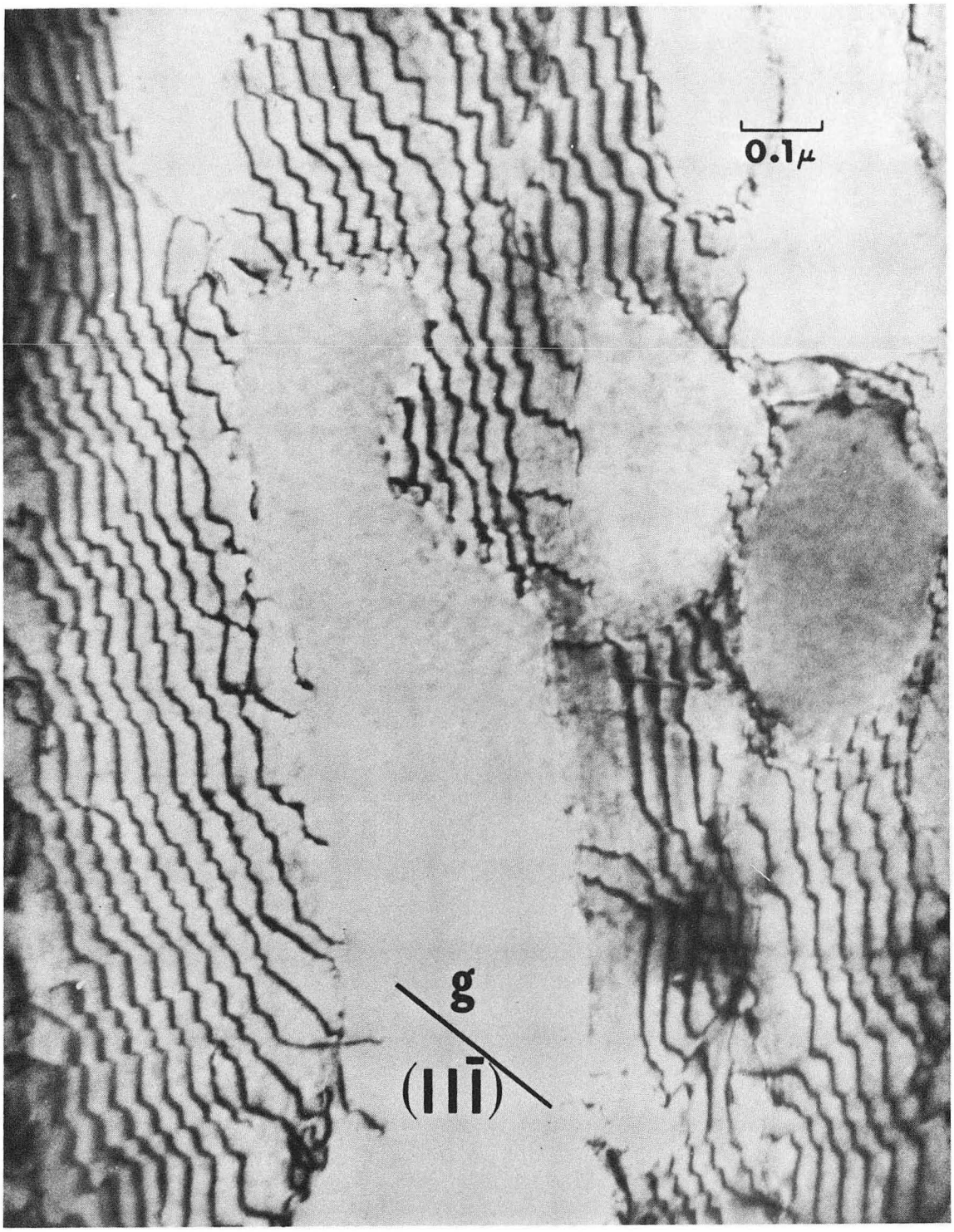

XBB 691-242

Fig. 13

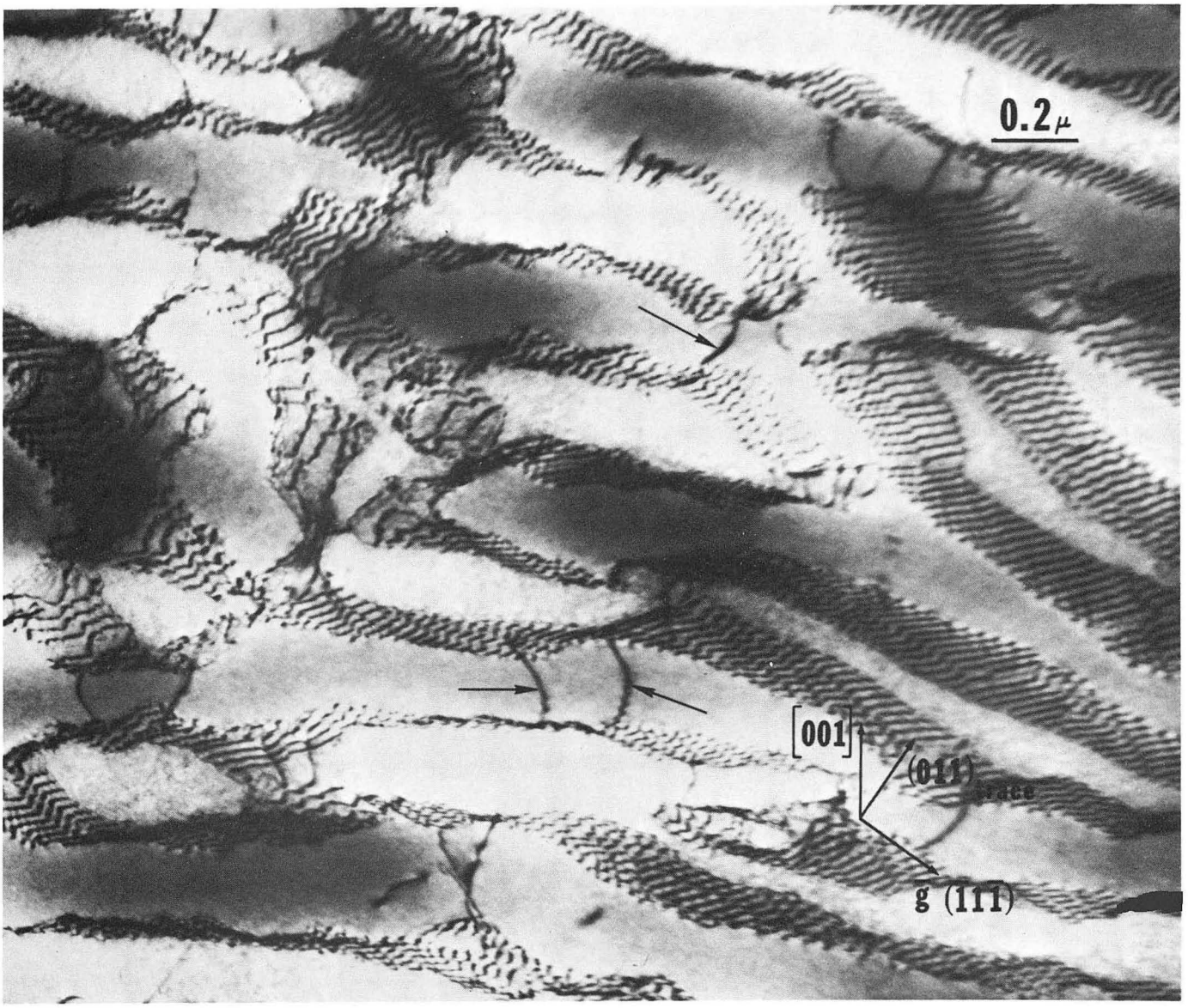

XBB 693-1866

Fig. 14

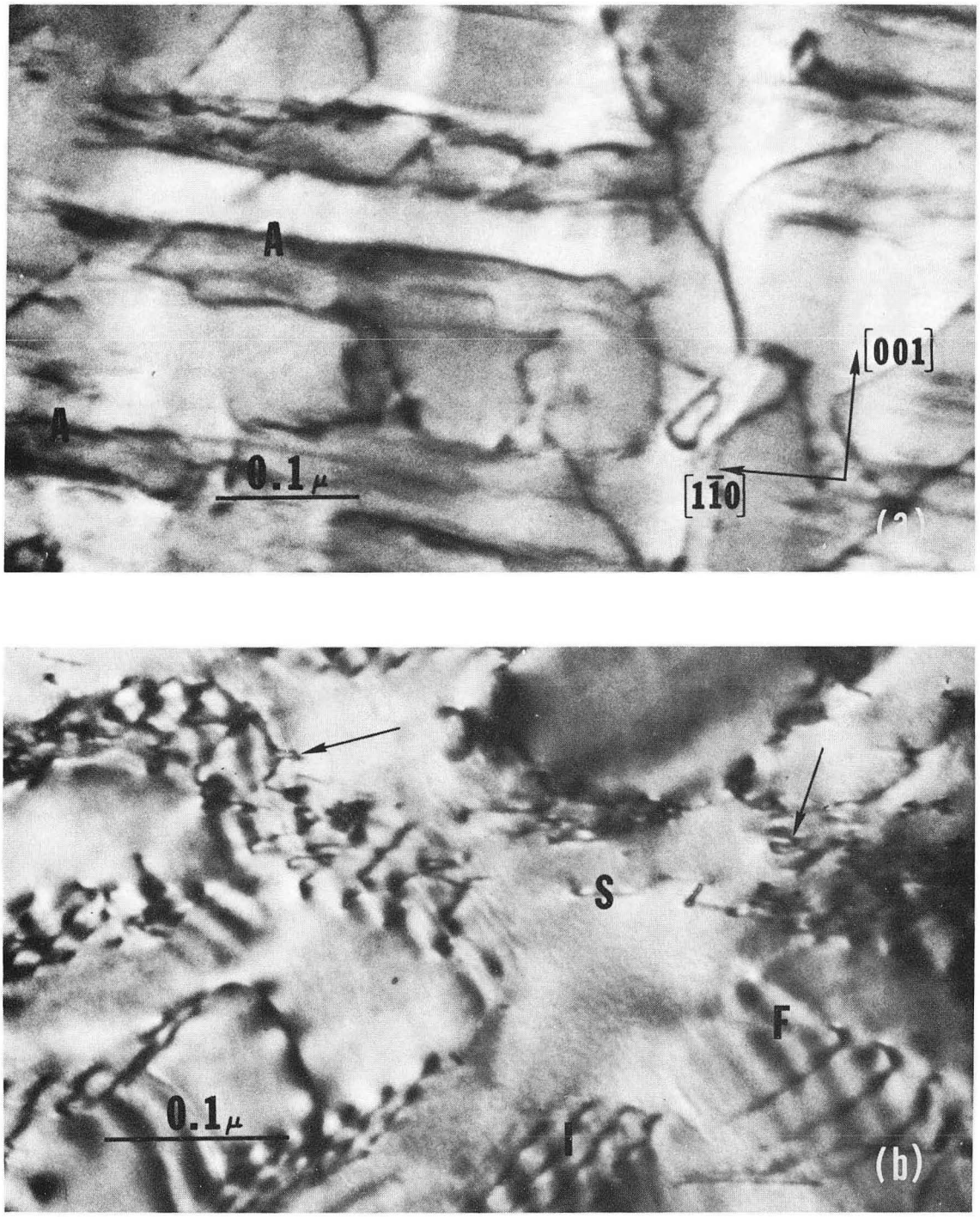

XBB 694-2457

Fig. 15

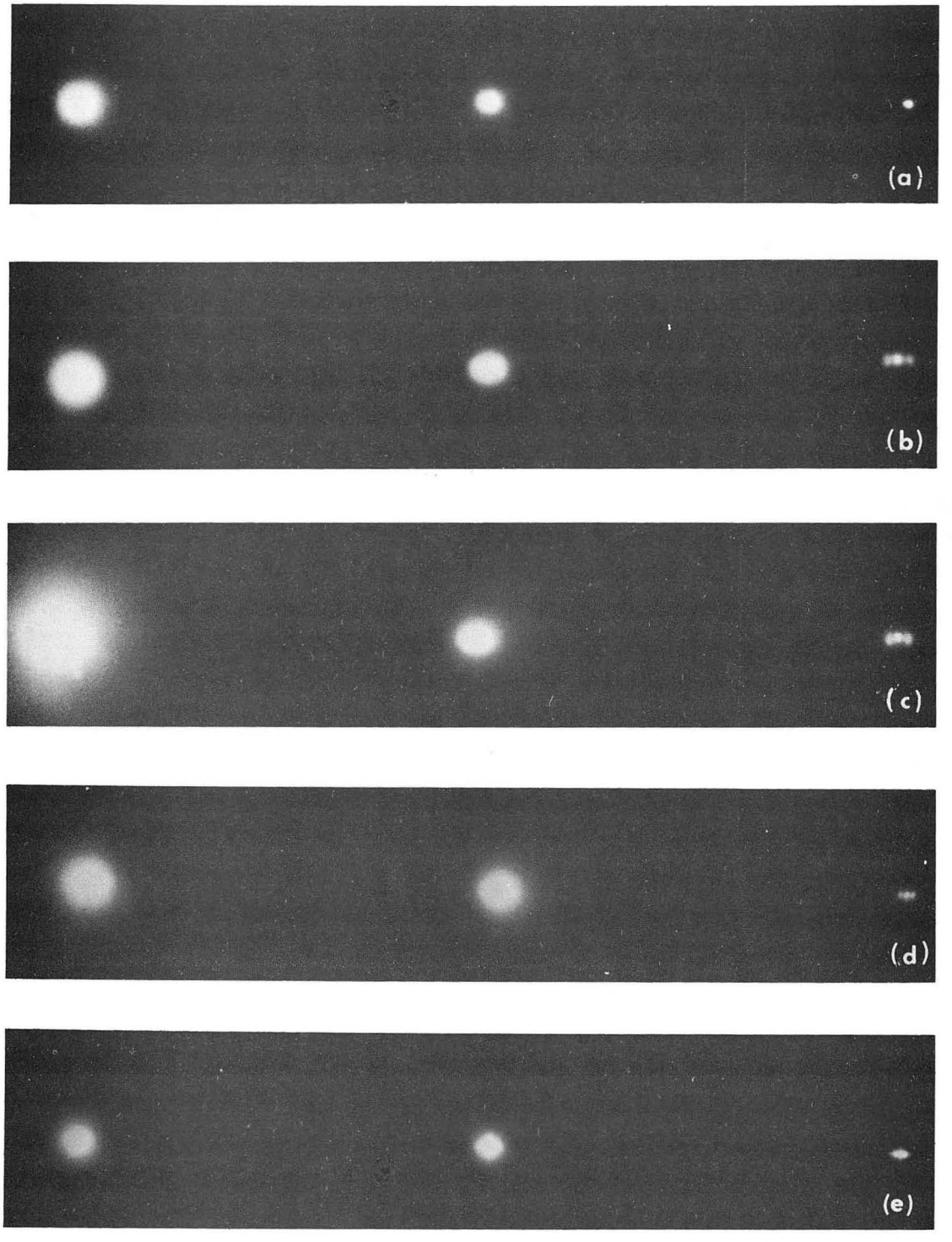

XBB 693-1857

Fig. 16

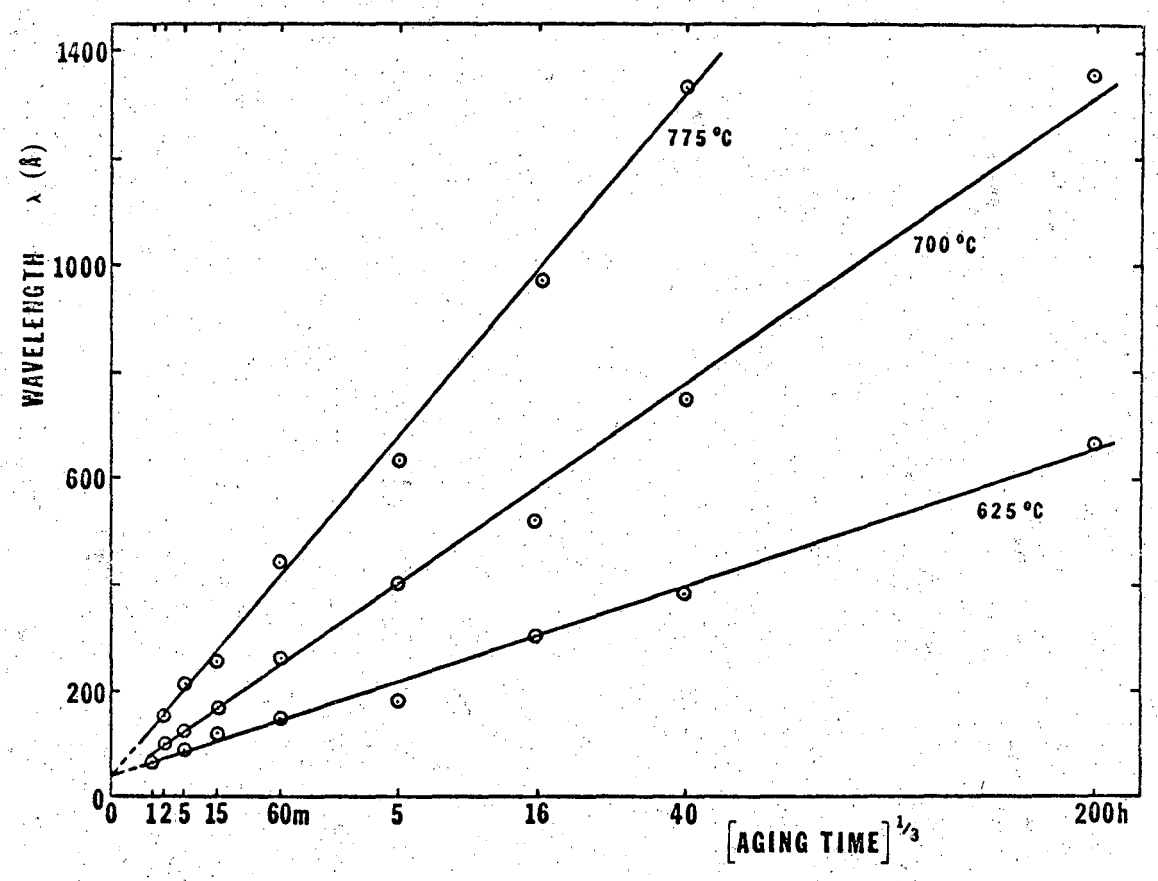

XBL 693-292

Fig. 17

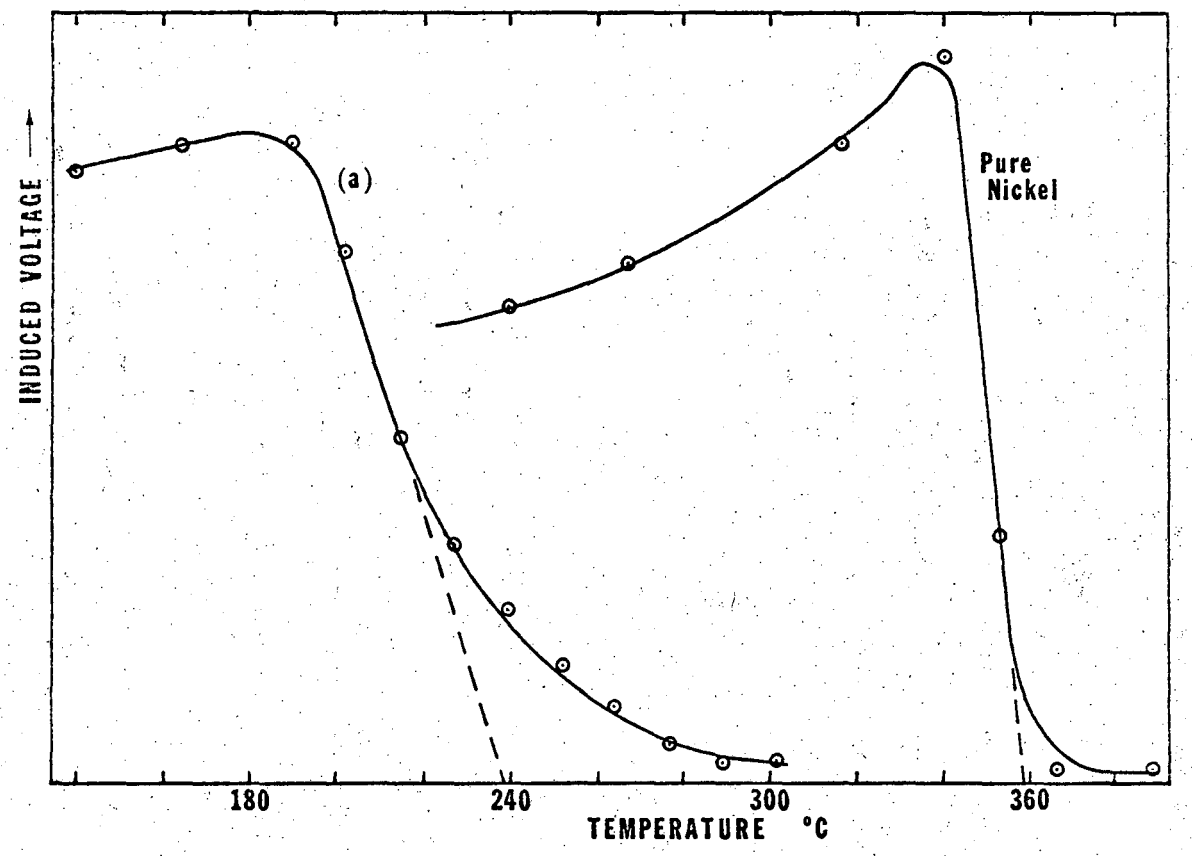

XBL 693-294

Fig. 18A

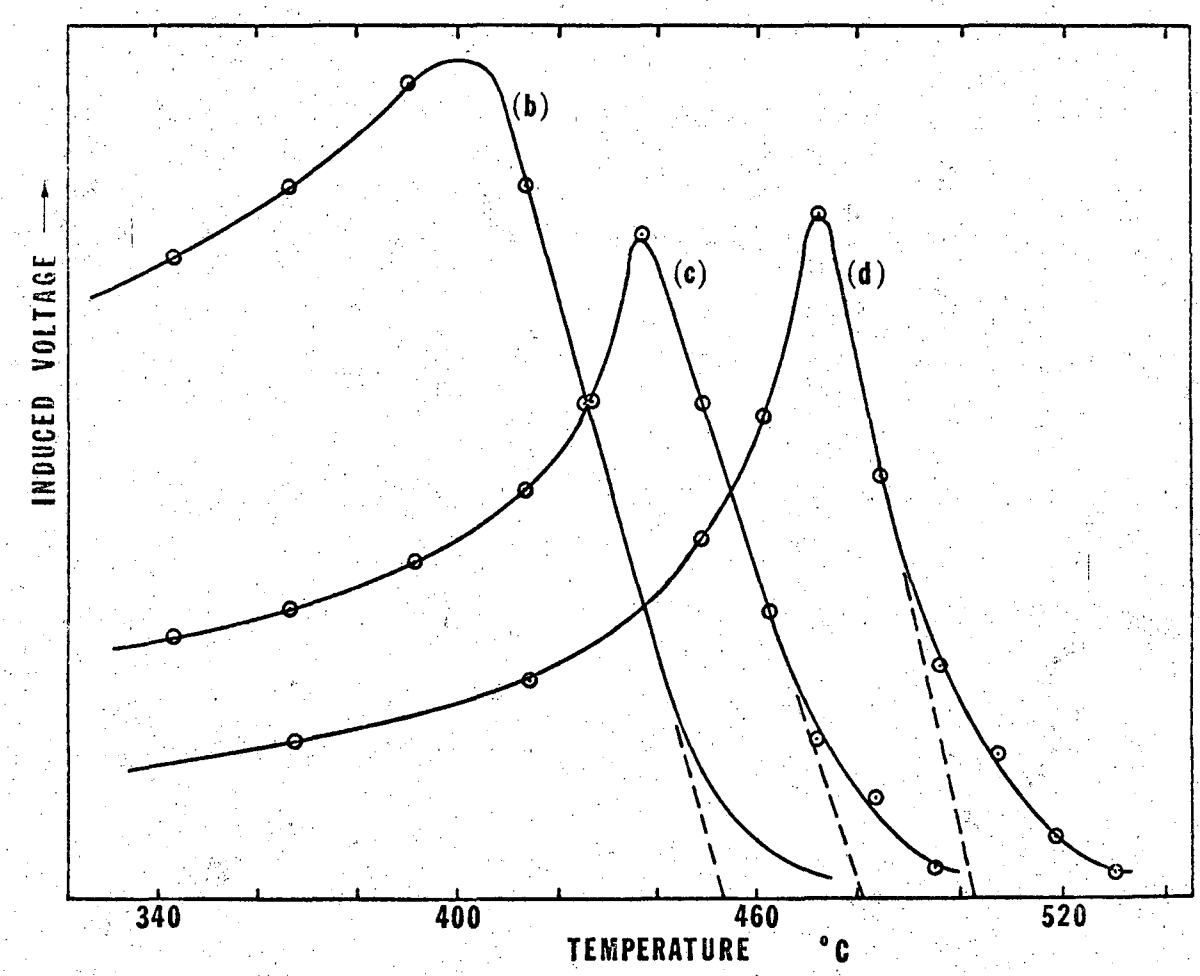

XBL 693-290

Fig. 18B

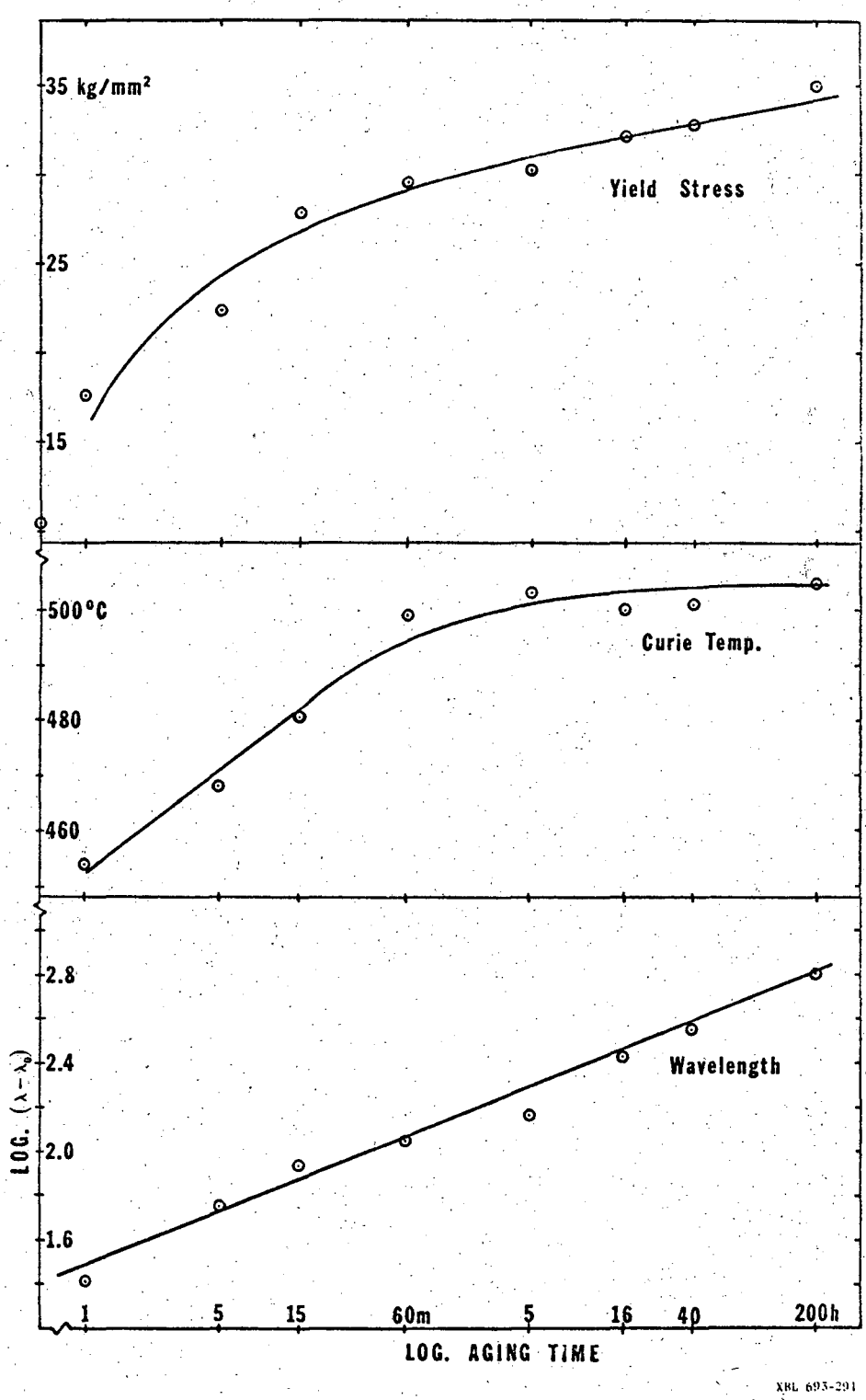
35 kg/mm²
25
15
Yield Stress
500°C
480
460
Curie Temp.
2.8
2.4
2.0
1.6
LOG. (λ-λ₀)
Wavelength
1
5
15
60m
5
16
40
200h
LOG. AGING TIME
XBL 693-291

Fig. 19

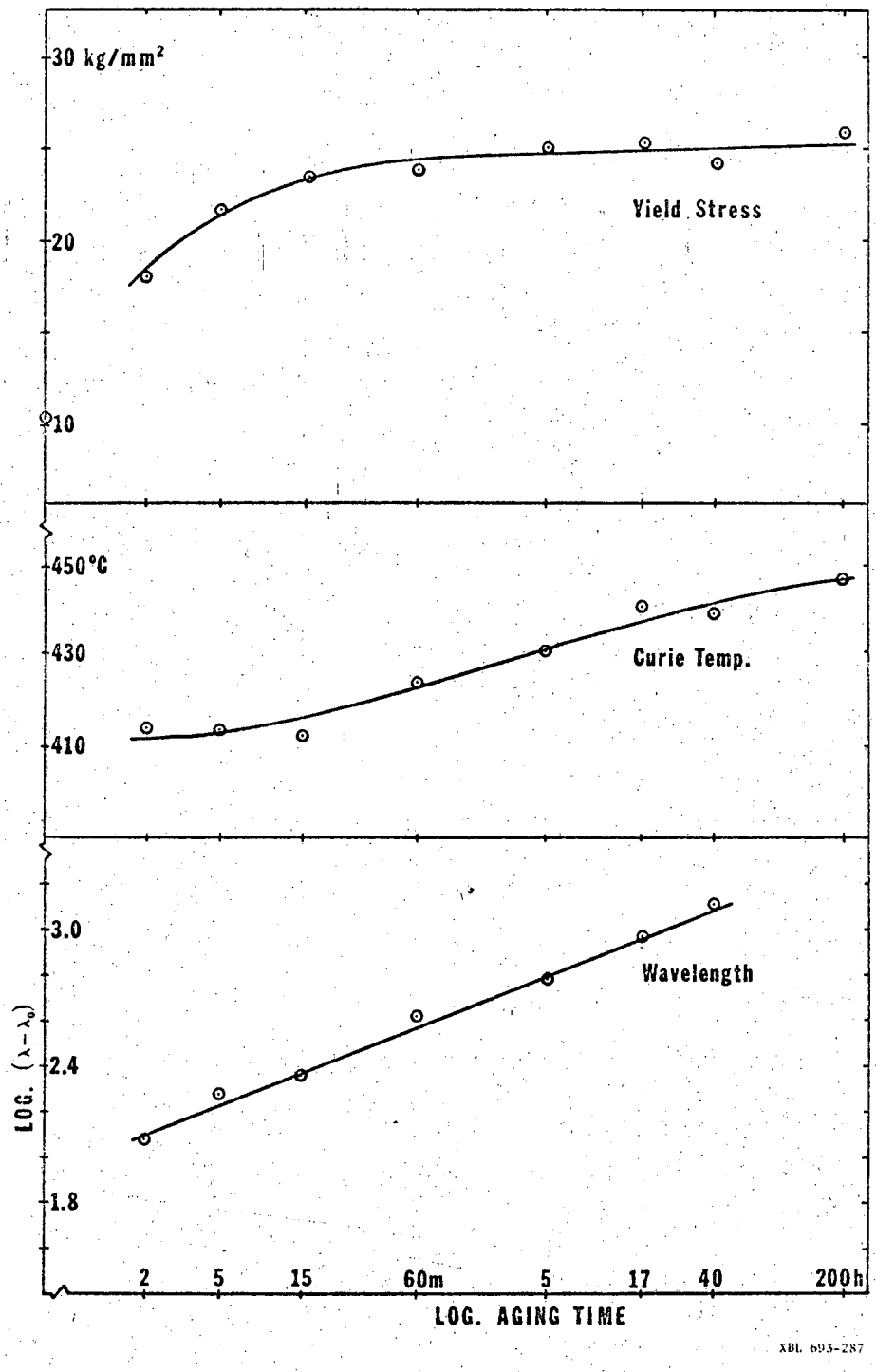
30 kg/mm²
20
10
Yield Stress
450°C
430
410
Curie Temp.
3.0
2.4
1.8
Wavelength
LOG. (λ−λ₀)
2
5
15
60m
5
17
40
200h
LOG. AGING TIME
XBL 693-287

Fig. 20

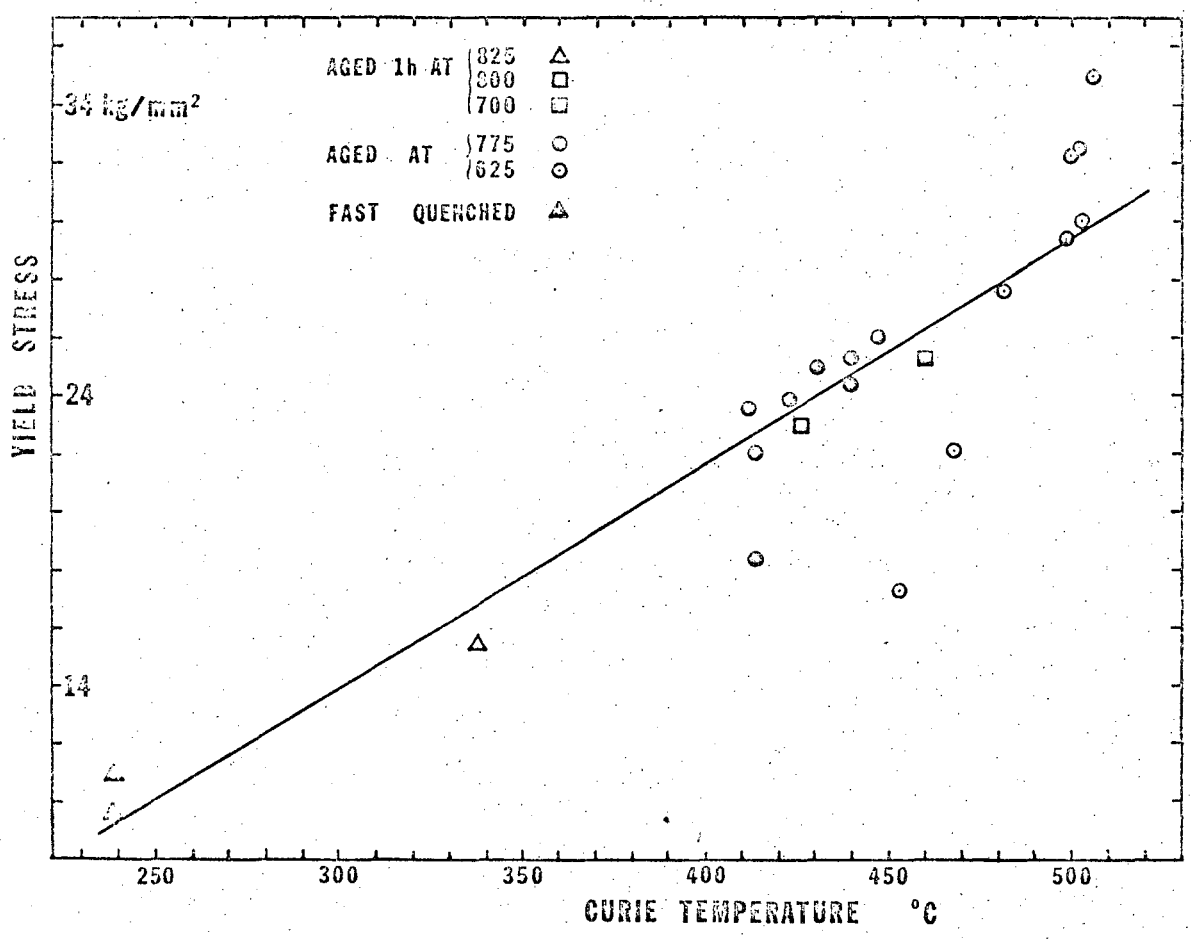

XBL 693-288

Fig. 21

LEGAL NOTICE

This report was prepared as an account of Government sponsored work. Neither the United States, nor the Commission, nor any person acting on behalf of the Commission:

A. Makes any warranty or representation, expressed or implied, with respect to the accuracy, completeness, or usefulness of the information contained in this report, or that the use of any information, apparatus, method, or process disclosed in this report may not infringe privately owned rights; or

B. Assumes any liabilities with respect to the use of, or for damages resulting from the use of any information, apparatus, method, or process disclosed in this report.

As used in the above, "person acting on behalf of the Commission" includes any employee or contractor of the Commission, or employee of such contractor, to the extent that such employee or contractor of the Commission, or employee of such contractor prepares, disseminates, or provides access to, any information pursuant to his employment or contract with the Commission, or his employment with such contractor.

TECHNICAL INFORMATION DIVISION
LAWRENCE RADIATION LABORATORY
UNIVERSITY OF CALIFORNIA
BERKELEY, CALIFORNIA 94720